

Neodymium Isotope Evidence for a Chondritic Composition of the Moon

K. Rankenburg,^{1*} A. D. Brandon,¹ C. R. Neal²

Samarium-neodymium isotope data for six lunar basalts show that the bulk Moon has a $^{142}\text{Nd}/^{144}\text{Nd}$ ratio that is indistinguishable from that of chondritic meteorites but is 20 parts per million less than most samples from Earth. The Sm/Nd formation interval of the lunar mantle from these data is 215_{-21}^{+23} million years after the onset of solar system condensation. Because both Earth and the Moon likely formed in the same region of the solar nebula, Earth should also have a chondritic bulk composition. In order to mass balance the Nd budget, these constraints require that a complementary reservoir with a lower $^{142}\text{Nd}/^{144}\text{Nd}$ value resides in Earth's mantle.

The most widely accepted theory for the formation of the Earth-Moon system proposes a giant impact model, where Earth collided in its later stages of accretion with a body of the approximate size of Mars (1, 2). In this model, the Moon ultimately formed from hot debris generated during this giant impact. Short-lived radioisotope systems such as ^{146}Sm - ^{142}Nd [half-life $t_{1/2} = 103$ million years (My)] are useful in determining the chronology of the events that formed the Earth-Moon system and for determining how these terrestrial bodies evolved after accretion. Recent Sm-Nd data show that chondritic meteorites are on average 20 parts per million (ppm) lower in $^{142}\text{Nd}/^{144}\text{Nd}$ than most terrestrial samples (3). If the bulk silicate Earth (BSE) has an Sm/Nd ratio within the range measured for chondrites, the superchondritic $^{142}\text{Nd}/^{144}\text{Nd}$ ratio of terrestrial materials requires that the silicate Earth experienced a global chemical differentiation during the lifetime of ^{146}Sm (~500 My). If this differentiation event is connected with the formation of the terrestrial depleted upper mantle, then it must have occurred no later than ~30 My after solar system formation (3). If the Moon has superchondritic $^{142}\text{Nd}/^{144}\text{Nd}$ similar to that of Earth's upper mantle, then the giant impact must have occurred into an already differentiated Earth, predominantly sampling the Nd-depleted reservoir. In order to test this hypothesis, we measured Nd-isotope ratios of six lunar basalts that span the compositional range of basaltic lavas from the Moon (4). Although anomalies in ^{142}Nd have been reported previously for lunar samples (5), the uncertainties in these data do not permit an evaluation of whether the bulk Moon is chondritic or instead identical to the terrestrial standard.

Core formation in planetesimals and terrestrial bodies likely occurred within ~30 My after formation of the solar nebula, based on ^{182}Hf - ^{182}W chronometry ($t_{1/2} = 9$ My) (6, 7). Core formation is independently indicated for

¹NASA Johnson Space Center, Mail Code KR, Houston, TX 77058, USA. ²Department of Civil Engineering and Geological Sciences, University of Notre Dame, Notre Dame, IN 46556, USA.

*To whom correspondence should be addressed. E-mail: kai.rankenburg1@jsc.nasa.gov

the impactor (termed Theia), because an undifferentiated projectile could not have produced an iron-poor Moon (8). Estimates for the timing of the giant impact on the basis of tungsten isotopes are model-dependent and range from ~30 My (9, 10) to at least 44 My after the formation of the solar system (11). A later age (≥ 50 My) for the formation of the Moon is more easily reconciled with the lunar initial $^{87}\text{Sr}/^{86}\text{Sr}$ ratio (12). Estimates for the crystallization of the putative lunar magma ocean (LMO), which are indicated by the crystallization age of materials strongly enriched with trace elements as the last remnants of the LMO (termed KREEP for K, potassium; REE, rare earth elements; and P, phosphorus), range from 30 to 50 My based on ^{182}Hf - ^{182}W data (13, 14) to ~250 My based on Sm-Nd data (5). The residual liquid at the end of LMO crystallization is also highly enriched in incompatible, heat-producing radionuclides such as ^{235}U and ^{40}K . This late-stage liquid could have acted as an insulating cover that substantially enhanced the longevity of the LMO (15).

Samarium and neodymium are refractory (i.e., they have high condensation temperatures) and lithophile elements (i.e., they preferentially partition in the silicate phase during core formation). Unlike the ^{182}Hf - ^{182}W system, which is influenced by core formation, the Sm-Nd isotope system is expected to record more reliably anomalies inherited from mantle sources with variable Sm/Nd ratios produced during global differentiation. However, because Earth is a geologically active planet, most variations initially present in

$^{142}\text{Nd}/^{144}\text{Nd}$ and $^{143}\text{Nd}/^{144}\text{Nd}$ from the early decay of ^{146}Sm and ^{147}Sm [$t_{1/2} = 106$ billion years (Gy)], respectively, have been subsequently homogenized. With the exception of only a few old crustal rocks (16, 17), all terrestrial samples have $\epsilon^{142}\text{Nd} = 0$ (18). The lunar samples studied here have crystallization ages of 3150 to 3900 My and preserve a range of present-day $\epsilon^{142}\text{Nd}$ from -0.30 ± 0.07 to $+0.07 \pm 0.05$ (errors are 2σ) when corrected for the effects of neutron irradiation (Fig. 1 and Table 1).

The source region of the low-Ti mare basalts (i.e., Apollo 15 sample 15555 and lunar meteorite LAP 02205) is postulated to consist mainly of olivine and orthopyroxene cumulates, formed early in a crystallizing LMO (19). The high-Ti mare basalt suite (i.e., Apollo 17 samples 70017 and 74275) is derived from Ti-rich mantle sources that contain additional cumulus ilmenite (20). This Ti-rich source may consist of deep mantle cumulates modified by varying degrees of hybridization and/or assimilation of formerly shallow material, swept down by a massive convective overturn of the lunar mantle (21, 22). Alternatively, this source may represent a relatively shallow late-stage cumulate pile containing trapped residual liquid and plagioclase (20).

The origin of the KREEP-rich samples 15386 and SaU 169 is less well constrained. They contain too much MgO to be derived directly from the hypothesized KREEP source that represents the residual liquid of the LMO. The KREEP signature of these basalts likely results from mixing between the KREEP source material and more magnesium-rich magmas derived from deeper mantle sources. Because of the high concentration of incompatible elements in KREEP, it will dominate the trace element and isotopic signature of a hybrid rock, whereas the major element chemistry (such as MgO content) will not be substantially changed.

We modeled the evolution of the lunar mantle for two situations. In the first model (Fig. 2, A and B), we assumed that the Moon formed by a giant impact from material with average chondritic composition with present-day $\epsilon^{143}\text{Nd} = 0$ and $\epsilon^{142}\text{Nd} = -0.2$ (3). The $\epsilon^{143}\text{Nd}$ and $\epsilon^{142}\text{Nd}$ of the evolving lunar mantle were calculated using a two-stage model (4). In

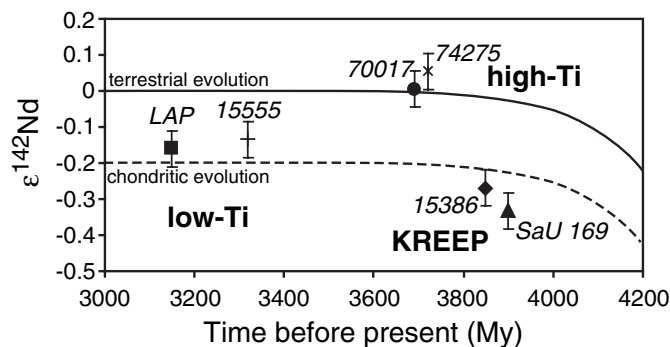


Fig. 1. Crystallization ages of the measured basalts versus their initial $\epsilon^{142}\text{Nd}$. Some lunar data have $\epsilon^{142}\text{Nd}$ values close to the terrestrial value, which has led to the suggestion that the Moon could have formed from a depleted portion of an early differentiated Earth's mantle (3).

the first stage, the LMO has a chondritic $^{147}\text{Sm}/^{144}\text{Nd}$ ratio until it is fractionated at time t_1 by the formation of a suite of contemporaneous lunar mantle rocks. The second stage marks melt extraction from the mantle and crystallization at time t_2 . The $(^{147}\text{Sm}/^{144}\text{Nd})_{t_1}$ ratio is calculated for each basalt source (table S6) from the initial $\epsilon^{143}\text{Nd}$ value ($\epsilon^{143}\text{Nd}_i$) and crystallization ages t_2 of the basalts (Table 1) and by setting t_1 arbitrarily to 50 and 200 My after formation of the solar system at $t_0 = 4567$ My (23). Plotting these values versus the measured present-day $\epsilon^{142}\text{Nd}$ for each time series t_1 forms linear arrays despite their disparate crystallization ages (Fig. 1). This suggests establishment of the sources of these lavas when ^{146}Sm was still alive. Although the choice of 50 or 200 My for the formation of the basalt sources from a chondritic LMO generates differences in the calculated source $^{147}\text{Sm}/^{144}\text{Nd}$ ratios, it does not greatly alter the slope of the best fit lines through the data (Fig. 2A). Self-consistent values of t_0 to t_1 and $(^{147}\text{Sm}/^{144}\text{Nd})_{t_1}$ were calculated for each sample by simultaneously solving equations S1 and S2 (4) for the two unknowns (Table 1). In this way, the combined ^{146}Sm and ^{147}Sm decay schemes constrain the source-formation age and its time-integrated $^{147}\text{Sm}/^{144}\text{Nd}$ ratio for each individual sample (24). An average of the source-formation times t_0 to t_1 (Table 1) was used to iteratively calculate $(^{147}\text{Sm}/^{144}\text{Nd})_{t_1}$ ratios until the slope of the regressed line matched the calculated ^{142}Nd isochron (Fig. 2A). A straightforward interpretation of this best fit solution (Fig. 2B) is that the lunar mantle sources represented by these samples formed at 215^{+23}_{-21} My after solar system formation. Assuming that the Moon formed 30 to 50 My after t_0 , a formation interval for the lunar mantle of $\sim 165^{+23}_{-21}$ to 185^{+23}_{-21} My is derived. This result is in agreement with the 238^{+56}_{-40} My formation interval obtained previously (5). However, our data intersect the chondritic $^{147}\text{Sm}/^{144}\text{Nd}$ ratio at $\epsilon^{142}\text{Nd} = -0.19 \pm 0.02$ [mean squared weighted deviation (MSWD) =

0.99], identical within error to the value of the chondritic uniform reservoir (CHUR) (3). Although this model suggests that a two-stage model is sufficient to explain the formation of the lunar samples represented in this study, it has been speculated that the Moon could have formed from a nonchondritic reservoir (3). Therefore, three- and four-stage models are discussed to constrain the conditions under which an initially nonchondritic bulk Moon could have generated the measured isotopic compositions of the lunar samples.

In the second model (Fig. 2C), the Moon was formed from material that predominantly sampled the Nd-depleted reservoir of an already differentiated Earth and/or impactor. In this case, $\epsilon^{143}\text{Nd}$ and $\epsilon^{142}\text{Nd}$ are calculated using a three-stage model (equations S3 and S4) in which $t_1 = 4537$ My and $(^{147}\text{Sm}/^{144}\text{Nd})_{t_1} = 0.2146$ (3), to yield a modern terrestrial depleted mantle reservoir with $\epsilon^{143}\text{Nd} = +10.7$ and $\epsilon^{142}\text{Nd} = 0$. Parameters t_2 and t_3 are then the times of LMO and basalt crystallization, respectively. Regressing calculated source $^{147}\text{Sm}/^{144}\text{Nd}$ ratios (table S6) versus present-day $\epsilon^{142}\text{Nd}$ yields a best fit $\epsilon^{142}\text{Nd}$ of -0.12 ± 0.02 (MSWD = 1.1) for a bulk Moon with $^{147}\text{Sm}/^{144}\text{Nd} = 0.2146$ (Fig. 2C). However, no calculated ^{142}Nd isochron fits the data in this model, because it also must pass through present-day $\epsilon^{142}\text{Nd} = 0$ (colored lines in Fig. 2C). This also explains the largely different individual source-formation ages calculated from combined $\epsilon^{142}\text{Nd}$ - $\epsilon^{143}\text{Nd}$ chronometry (Table 1). The low-Ti and high-Ti sources yield either unreasonably low (0^{+62} My) or high (761^{+50}_{-358} My) values for the formation interval t_1 to t_0 , respectively.

The datum for 15555, in particular, implies that the Moon has a chondritic mantle with respect to Nd isotopes, because its initial $\epsilon^{143}\text{Nd}$ value is more precisely constrained from an internal isochron (5). For a depleted starting composition, 15555 plots outside the range of possible $\epsilon^{142}\text{Nd}$ - $\epsilon^{143}\text{Nd}$ compositions (Fig. 3). In addition, the Nd isotopic composition of

15555 cannot be interpreted as mixing between KREEP with low $^{147}\text{Sm}/^{144}\text{Nd}$ and depleted lunar mantle with high $^{147}\text{Sm}/^{144}\text{Nd}$ (Fig. 3), because formation of the KREEP source must equal or postdate the formation of the depleted source. To explain these data within the context of an initially depleted Nd isotopic composition for the Moon, a more complicated four-stage model can be constructed, where the depleted starting material is enriched during early differentiation of the LMO [e.g., at 40 My with $(^{147}\text{Sm}/^{144}\text{Nd})_{t_2} = 0.1985$]. Internal differentiation of such a re-enriched LMO at $t_3 = 215$ My with $(^{147}\text{Sm}/^{144}\text{Nd})_{t_3} = 0.217$ could then form a suitable source for sample 15555. However, because of Nd mass-balancing requirements, the additional stage in the model calls for a complementary reservoir of lunar mantle cumulates with, depending on its size, highly depleted Nd isotope compositions. Because such a reservoir is as yet not represented in the lunar sample collection, the hypothesis of an initially depleted Moon is unlikely. If the correlation between $\epsilon^{142}\text{Nd}$ and source $^{147}\text{Sm}/^{144}\text{Nd}$ ratio (Fig. 2B) represents an isochron and not a mixing line, then the age derived from the chondritic model most probably dates the last global lunar mantle re-equilibration. In this context, these Nd isotope data demonstrate that the LMO has a negative present-day $\epsilon^{142}\text{Nd}$ and was not formed entirely from depleted portions of Earth's and/or the impactor's mantle.

The lunar source-formation age of 215^{+23}_{-21} My calculated from Nd isotopes within the context of an initially chondritic Moon is inconsistent with a proposed LMO crystallization age of only 30 to 50 My obtained from ^{182}Hf - ^{182}W systematics (13, 14). For example, low-Ti basalt 15555, used to pinpoint the bulk lunar $^{182}\text{W}/^{184}\text{W}$ (13) provides an Nd source-formation age of 221^{+264}_{-98} My. Moreover, the nonchondritic $^{147}\text{Sm}/^{144}\text{Nd}$ ratio of 0.218 calculated for the 15555 source (Table 1) violates the assumption of an undifferentiated Hf-W ratio (13). Average model ages for KREEP are $4.42 \pm$

Table 1. Nd and Sm isotope data measured in this study. NS, no solution. Crystallization ages and radiometric system from the literature as follows: SaU 169 (Pb-Pb) from (38); 15386 (Sm-Nd) from (5); 70017, 74275 (average of groups B and C from multiple methods) from (39); 15555 (Sm-Nd) from (40). Corr., neutron fluence corrected. Src., source.

Sample	Weight (mg)	$\epsilon^{142}\text{Nd}$	$\epsilon^{143}\text{Nd}$	$\epsilon^{149}\text{Sm}$	$\epsilon^{142}\text{Nd}$ corr.	$\epsilon^{143}\text{Nd}$ corr.	Age (My)	Sm (ppm)	Nd (ppm)	$^{147}\text{Sm}/^{144}\text{Nd}$	$\epsilon^{142}\text{Nd}_i$	$\epsilon^{143}\text{Nd}_i$	t_0 to t_1 CHUR	$^{147}\text{Sm}/^{144}\text{Nd}$ CHUR src.	t_0 to t_1 DLM	$^{147}\text{Sm}/^{144}\text{Nd}$ DLM src.
LAP 02205	43 to 127	-0.18	0.65	-3.5	-0.16	0.68	3150*	5.82	17.9	0.1963	-0.16	1.1*	113^{+50}_{-113}	0.2028	0^{+62}	0.2026
$2\sigma \pm$ ($n = 7$)		0.04	0.03		0.04											
SAU 169	11.98	-0.32	-16.48	-12.5	-0.30	-16.37	3900	61.8	221.5	0.1688	-0.34	-2.5	233^{+353}_{-116}	0.1529	128^{+68}_{-49}	0.1581
$2\sigma \pm$ ($n = 2$)		0.05	0.05		0.07											
15386	22.60	-0.34	-16.35	-32.5	-0.24	-16.06	3850	34.5	122.7	0.1699	-0.27	-1.22*	243^{+50}_{-203}	0.1769	93^{+87}_{-58}	0.1798
$2\sigma \pm$ ($n = 3$)		0.05	0.06		0.07											
74275	54.70	0.06	30.06	-1.9	0.07	30.08	3720	13.1	32.0	0.2470	0.06	5.8	178^{+39}_{-33}	0.2619	372^{+50}_{-114}	0.2757
70017	59.24	0.01	40.64	-1.4	0.02	40.65	3690	5.19	11.7	0.2681	0.01	6.5	232^{+51}_{-39}	0.2726	761^{+50}_{-358}	0.5069
15555	139.90	-0.16	4.71	-5.3	-0.14	4.76	3320	2.70	8.09	0.2017	-0.14	2.88*	221^{+264}_{-98}	0.2177	NS	NS
Allende	1002.30	-0.41	-0.91	-0.6	-0.41	-0.91										

*From internal isochron.

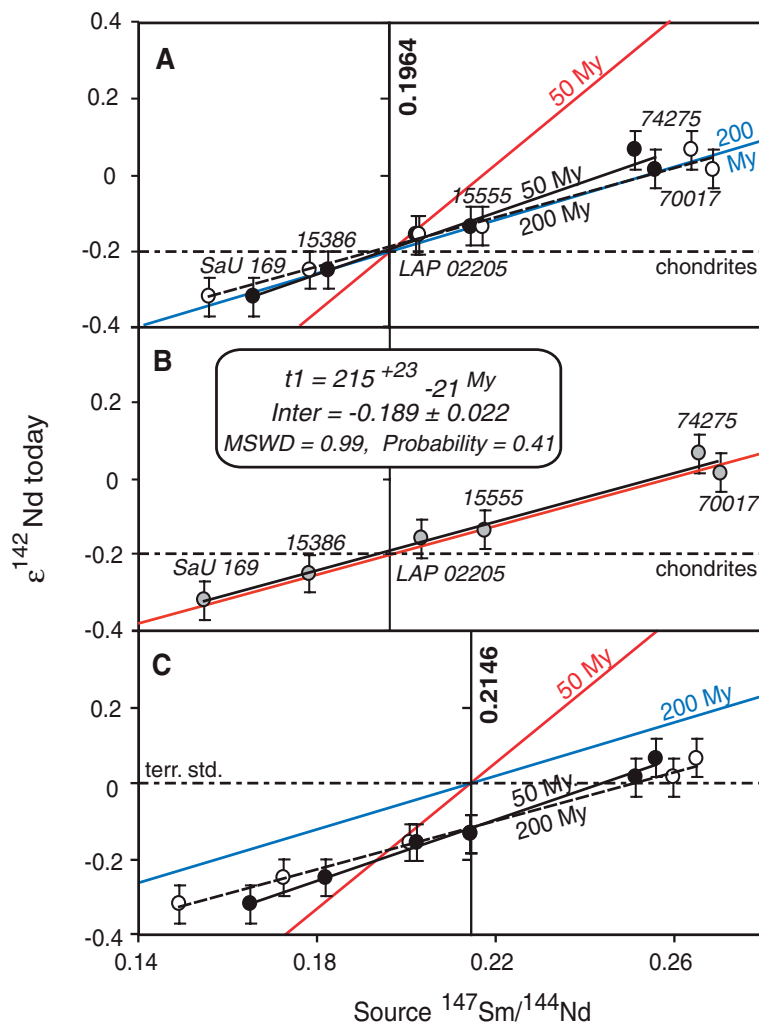
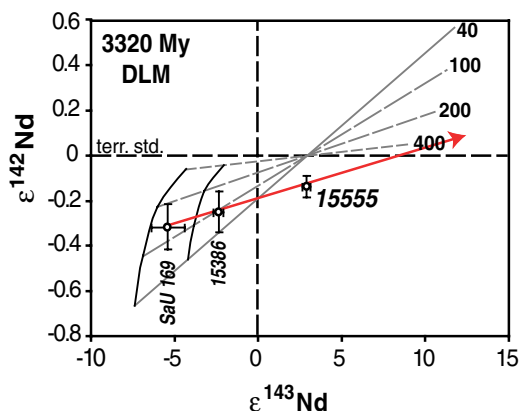


Fig. 2. (A) Illustration of the interaction of $^{147}\text{Sm}/^{144}\text{Nd}$, $\epsilon^{142}\text{Nd}$, and $\epsilon^{143}\text{Nd}$. Source $^{147}\text{Sm}/^{144}\text{Nd}$ ratios for each sample (table S6) plotted versus measured present-day $\epsilon^{142}\text{Nd}$ along with regression lines for each source-formation age (black lines). Also shown are ^{142}Nd -isochrons calculated for reservoirs formed from a chondritic LMO at 50 and 200 My after t_0 (labeled colored lines) using $^{147}\text{Sm}/^{144}\text{Nd} = 0.1964$, $^{146}\text{Sm}/^{144}\text{Sm} = 0.0075$ at 4567 My, and $\lambda^{146}\text{Sm} = 6.74 \times 10^{-9} \text{ year}^{-1}$. (B) A self-consistent model is obtained for $t_1 = 215^{+23}_{-21} \text{ My}$. The present-day bulk lunar $\epsilon^{142}\text{Nd}$ from this model is -0.19 ± 0.02 , similar to that of chondrites (3). (C) Same samples as before, but calculated as three-stage model (4), in which the Moon was formed from a depleted source. The depletion age of 4537 My and $^{147}\text{Sm}/^{144}\text{Nd} = 0.2146$ correspond to a model which forms the terrestrial mid-ocean ridge basalt source with present-day $\epsilon^{142}\text{Nd} = 0$ and $\epsilon^{143}\text{Nd} = 10.69$ (3).

Fig. 3. Snapshot of $^{142,143}\text{Nd}$ isotopic evolution along with isochrons for sources formed from an initially depleted lunar mantle source (DLM) at $t = 40, 100, 200, 400 \text{ My}$ after solar system formation (labeled lines). In this model, low-Ti basalt 15555 plots outside the range of possible $\epsilon^{142}\text{Nd}$ - $\epsilon^{143}\text{Nd}$ compositions. The composition of 15555 cannot be interpreted as mixing between low $^{147}\text{Sm}/^{144}\text{Nd}$ KREEP (15386 and SaU 169 sources are projected to 3320 My) and depleted high $^{147}\text{Sm}/^{144}\text{Nd}$ lunar mantle, because the formation of the KREEP source must equal or postdate formation of the depleted source; i.e., no mixing line (arrow) can be drawn connecting a KREEP reservoir, sample 15555, and a depleted reservoir that is younger than KREEP.



0.14 (2σ) Gy from ^{87}Rb - ^{87}Sr (25), $\sim 4.42 \text{ Gy}$ from $^{238,235}\text{U}$ - $^{206,207}\text{Pb}$ (26), and $\sim 4.36 \text{ Gy}$ from ^{143}Sm - ^{144}Nd isotope systematics (27) and have been interpreted to represent the final crystallization of the LMO (28). The age presented here overlaps this range and is consistent with other results from Nd isotopes (5).

Models of planetesimal accretion suggest that the impactor formed close to Earth (29), which is in accordance with measured oxygen and chromium isotopes of Earth and the Moon (30, 31). Numerical simulations of the giant impact suggest that $\sim 80\%$ of the lunar mass was derived from the impactor's mantle, the rest from Earth (32). This expectation is difficult to reconcile with a similar nonchondritic lunar and terrestrial $\epsilon^{142}\text{Nd}$, unless the impactor had a similar history of silicate differentiation to Earth (3). Our finding that the Moon was formed from a chondritic reservoir is consistent with other compositional indicators of a chondritic LMO, such as the flat REE patterns inferred for parental liquids of the lunar ferroan anorthosites (FANs) constituting the lunar crust, and superchondritic rather than subchondritic Ba/Sr in FAN plagioclases (33). If Earth and the Moon formed close to each other, it is likely that the bulk Earth also formed with a chondritic $^{147}\text{Sm}/^{144}\text{Nd}$ ratio. Hence, in order to balance the Nd budget of the sampled terrestrial reservoirs having $\epsilon^{142}\text{Nd} = 0$, to obtain a bulk chondritic composition of $\epsilon^{142}\text{Nd} \sim -0.20$, an isolated enriched mantle reservoir must reside somewhere in the present Earth (34–36). Initial differentiation could result from an early formed dense phase with higher compatibility for Nd than Sm, or deep subduction of early-formed crust (33). Such reservoirs are predicted to reside in the interface layer (D'') between Earth's silicate mantle and its metallic core (34–37).

The conclusion that the Moon has $\epsilon^{142}\text{Nd}$ close to the chondritic value does not, however, constrain the relative timing of giant impact and early silicate fractionation on Earth. Assuming that approximately 80% of the Moon-forming material was derived from a chondritic impactor and 20% from a hypothetical depleted Earth reservoir with present-day $\epsilon^{142}\text{Nd} = 0$, the measured lunar $\epsilon^{142}\text{Nd}$ of -0.19 could be achieved if chondrites have an average $\epsilon^{142}\text{Nd}$ of -0.24 , which is well within error limits of measured chondritic values (3).

References and Notes

1. W. K. Hartmann, D. R. Davis, *Icarus* **24**, 504 (1975).
2. R. M. Canup, *Icarus* **168**, 433 (2004).
3. M. Boyet, R. W. Carlson, *Science* **309**, 576 (2005).
4. Materials and methods are available as supporting material on Science Online.
5. L. E. Nyquist *et al.*, *Geochim. Cosmochim. Acta.* **59**, 2817 (1995).
6. T. Kleine, C. Münker, K. Mezger, H. Palme, *Nature* **418**, 952 (2002).
7. Q. Yin *et al.*, *Nature* **418**, 949 (2002).
8. H. Palme, *Science* **304**, 977 (2004).
9. S. B. Jacobsen, Q. Z. Yin, *Proc. Lun. Planet. Sci. Conf.* **34**, 1913 (2003).

10. T. Kleine, K. Mezger, C. Münker, *Proc. Met. Soc.* **66**, 5212 (2003).
11. A. N. Halliday, *Nature* **427**, 505 (2004).
12. A. N. Halliday, D. Pocielli, *Earth Planet. Sci. Lett.* **192**, 545 (2001).
13. T. Kleine, H. Palme, K. Mezger, A. N. Halliday, *Science* **310**, 1671 (2005).
14. C. K. Shearer, H. E. Newsom, *Geochim. Cosmochim. Acta.* **64**, 3599 (2000).
15. P. C. Hess, E. M. Parmentier, *J. Geophys. Res.* **E106**, 28 (2001).
16. G. Caro, B. Bourdon, J.-L. Birck, S. Moorbath, *Geochim. Cosmochim. Acta.* **70**, 164 (2006).
17. M. Boyet et al., *Earth Planet. Sci. Lett.* **214**, 427 (2003).
18. Variations from the terrestrial standard are expressed as $\epsilon^{142}\text{Nd} = \left[\frac{(^{142}\text{Nd}/^{144}\text{Nd})_{\text{sample}}}{(^{142}\text{Nd}/^{144}\text{Nd})_{\text{terr.std}}} - 1 \right] \times 10^4$; variations in $^{143}\text{Nd}/^{144}\text{Nd}$ are expressed as deviations from the evolution of the CHUR as $\epsilon^{143}\text{Nd} = \left[\frac{(^{143}\text{Nd}/^{144}\text{Nd})_{\text{sample}}}{(^{143}\text{Nd}/^{144}\text{Nd})_{\text{CHUR}}} - 1 \right] \times 10^4$.
19. L. T. Elkins-Tanton, N. Chatterjee, T. L. Grove, *Meteor. Planet. Sci.* **38**, 515 (2003).
20. G. A. Snyder, L. A. Taylor, C. R. Neal, *Geochim. Cosmochim. Acta.* **56**, 3809 (1992).
21. A. E. Ringwood, S. E. Kesson, *Proc. Lun. Sci. Conf.* **7**, 1697 (1976).
22. L. T. Elkins-Tanton, J. A. Van Orman, B. H. Hager, T. L. Grove, *Earth Planet. Sci. Lett.* **196**, 239 (2002).
23. Y. Amelin, A. N. Krot, I. D. Hutcheon, A. A. Ulyanov, *Science* **297**, 1678 (2002).
24. C. L. Harper, S. B. Jacobsen, *Nature* **360**, 728 (1992).
25. L. E. Nyquist, C. Y. Shih, *Geochim. Cosmochim. Acta.* **56**, 2213 (1992).
26. F. Tera, G. J. Wasserburg, *Proc. Lun. Sci. Conf.* **5**, 571 (1974).
27. R. W. Carlson, G. W. Lugmair, *Earth Planet. Sci. Lett.* **45**, 123 (1979).
28. G. A. Snyder, L. E. Borg, L. E. Nyquist, L. A. Taylor, in *Origin of the Earth and Moon*, R. M. Canup, K. Righter, Eds. (Univ. Arizona Press, Tucson, 2000), pp. 361–396.
29. G. W. Wetherill, in *Origin of the Moon*, W. K. Hartmann, R. J. Phillips, G. J. Taylor, Eds. (LPI, Houston, TX, 1986), pp. 519–550.
30. U. Wiechert et al., *Science* **294**, 345 (2001).
31. G. W. Lugmair, A. Shukryukov, *Geochim. Cosmochim. Acta.* **62**, 2863 (1998).
32. R. M. Canup, *Annu. Rev. Astron. Astrophys.* **42**, 441 (2004).
33. M. D. Norman, L. E. Borg, L. E. Nyquist, D. E. Bogard, *Meteor. Planet. Sci.* **38**, 645 (2003).
34. I. Tolstikhin, A. W. Hofmann, *Phys. Earth. Planet. Int.* **148**, 109 (2005).
35. T. W. Becker, J. B. Kellogg, R. J. O'Connell, *Earth Planet. Sci. Lett.* **171**, 351 (1999).
36. L. H. Kellogg, B. H. Hager, R. D. Van der Hilst, *Science* **283**, 1881 (1999).
37. G. Caro, B. Bourdon, B. J. Wood, A. Corgne, *Nature* **436**, 246 (2005).
38. E. Gnos et al., *Science* **305**, 657 (2004).
39. J. B. Paces et al., *Geochim. Cosmochim. Acta.* **55**, 2025 (1991).
40. L. E. Nyquist et al., *Proc. Lun. Planet. Sci. Conf.* **22**, 985 (1991).
41. This work was done under a postdoctoral research appointment at NASA managed by the National Research Council, and NASA Cosmochemistry grants to A.D.B. and C.R.N. Sample SaU 169 was kindly provided by B. Hofmann at the Natural History Museum Bern, Switzerland. LAP 02205 and Apollo rocks were supplied by Astromaterials and Research Exploration Science Directorate at NASA-JSC. The comments of S. Berthet, M. Sharma and one anonymous reviewer greatly helped to improve former versions of this paper.

Supporting Online Material

www.sciencemag.org/cgi/content/full/312/5778/1369/DC1

Materials and Methods

SOM Text

Figs. S1 to S11

Tables S1 to S6

References

9 February 2006; accepted 19 April 2006

10.1126/science.1126114

Early Domesticated Fig in the Jordan Valley

Mordechai E. Kislev,^{1*} Anat Hartmann,² Ofer Bar-Yosef³

It is generally accepted that the fig tree was domesticated in the Near East some 6500 years ago. Here we report the discovery of nine carbonized fig fruits and hundreds of drupelets stored in Gilgal I, an early Neolithic village, located in the Lower Jordan Valley, which dates to 11,400 to 11,200 years ago. We suggest that these edible fruits were gathered from parthenocarpic trees grown from intentionally planted branches. Hence, fig trees could have been the first domesticated plant of the Neolithic Revolution, which preceded cereal domestication by about a thousand years.

New archaeobotanic evidence seems to indicate that fig cultivation was widely practiced in the Near East during the 12th millennium before the present (B.P.), nearly a thousand years before the domestication of cereals and legumes. The origin of the common fig (*Ficus carica*) is still an unsettled issue, though some of its major steps have been reconstructed (1–6). Finds include fruit fragments and drupelets from Gilgal I (Fig. 1 and figs. S1 to S3), an early Neolithic site in the Jordan Valley, as well as from a number of other Neolithic sites of similar age (1, 7–11). Figs in these early archaeological sites significantly outnumber any other fruit remains from that period. This successful human initiation was probably due to the simplicity of fig tree propagation, which is achieved by merely cutting and planting branches (12). Small genetic changes in wild figs occurring

at that time considerably improved the fruit's taste. These two characters may explain why the domestication of the fig preceded that of other fruit trees, such as the grape, olive, and date, by almost five millennia (13).

The common fig is a gynodioecious species composed of two sexes: the hermaphroditic inedible caprifig, which is functionally a male fig (*F. carica* var. *caprificus*), and the edible female seed fig (*F. carica* var. *domestica*). The hermaphroditic tree produces both male staminate flowers and female pistillate flowers within each fig syconium, whereas the female variety has only pistillate flowers. There is also a widely grown parthenocarpic variety of

female fig, in which the ovaries develop into drupelets without pollination and fertilization.

The fig tree, whose fertilization is carried out by the symbiotic fig wasp *Blastophaga psenes* (fig. S4), produces three crops during the year: in early summer (June–July), in midsummer-autumn (August–November), and in early spring (March). The polleniferous spring hermaphroditic figs are the main source of wasp-borne pollen, but the syconia of the remaining two crops produce little or no fertile pollen. They function as domiciles in which the short-lived wasps propagate (14).

The syconium is an enclosed inflorescence that transforms into a hollow receptacle. Whereas the syconia of the hermaphroditic caprifig produce minute staminate flowers and pistillate flowers with a short style (2 mm long), the syconia of the female fig tree produce only long-style (3 mm long) pistillate flowers. Style length has a crucial role in the fertilization process, because the minute fig wasp has an ovipositor 2 mm long. After emerging from its native syconium, the flying wasp, coated with pollen, enters through the orifice (ostiole) of a young syconium on a different tree. When meeting the short-style flower in a hermaphroditic tree, the wasp successfully inserts its egg through the style into the flower's ovary. As a result, a larva develops that feeds on the developing tissue and emerges through a hole in

Table 1. Early Neolithic (11,500 to 10,300 years B.P.) fig remains in the Levant.

Site	Region	Calendar years B.P.	Quantity*
Jericho Phase VIIB (7, 21)	Jordan Valley	11,400–10,500	1 + 46
Gilgal I	Jordan Valley	11,400–11,200	9 + 313
Gilgal III	Jordan Valley	11,700–11,260	1 + 30
Netiv Hagdud (8)	Jordan Valley	11,300–10,900	1 + 4913
Gesher (9, 21)	Jordan Valley	11,300	36
Mureybit Phase III (10)	Euphrates Valley	11,400–10,600	1 + 3

*Bold text, fruit fragments; normal text, drupelets.

¹Faculty of Life Sciences, Bar-Ilan University, 52900 Ramat-Gan, Israel. ²Land of Israel Studies and Archaeology Department, Bar-Ilan University, 52900 Ramat-Gan, Israel. ³Department of Anthropology, Peabody Museum, Harvard University, Cambridge, MA 02138, USA.

*To whom correspondence should be addressed. E-mail: kislev@mail.biu.ac.il



Supporting Online Material for
**Neodymium Isotope Evidence for a Chondritic Composition of the
Moon**

K. Rankenburg,^{1*} A. D. Brandon,¹ C. R. Neal²

*To whom correspondence should be addressed. E-mail: kai.rankenburg1@jsc.nasa.gov

Published 2 June 2006, *Science* **312**, 1369 (2006)
DOI: 10.1126/science.1126114

This PDF file includes:

Materials and Methods

SOM Text

Figs. S1 to S11

Tables S1 to S6

References

Supporting Online Material:

Sample preparation and analytical techniques

Four Apollo mare basalts (15555,923; 70017,517; 74275,316; 15386,48), two lunar meteorites (LAP 02205,23; Sayh al Uhaymir 169) and the CI chondrite Allende, were analyzed for their Sm and Nd isotope compositions (IC). An aliquot of each whole rock sample equivalent to 1-2 microgram of total neodymium (10-140 mg; depending on Nd concentration) was first inspected for visible surface contamination under a binocular microscope. Lunar meteorite SaU 169, found in the Sultanate of Oman (1), was the only rock with visible terrestrial alteration. To remove traces of secondary carbonate, the sample was cleaned ultrasonically for 15 min in 50% acetic acid and Milli-Q® water. All samples were then crushed by hand in a boron carbide mortar and pestle and set aside for whole rock isotope analysis. Between the samples, the mortar was cleaned with Milli-Q® water and alcohol. For lunar meteorite LAP 02205, a larger aliquot of 944 mg was ground to <100 mesh. One fourth of the material (219.08 mg) was used for multiple bulk rock analysis. The remaining sample material was saved for isochron work (2). Sample powders were subsequently leached for 10 min in H₂O and cold 1N HCl in an ultrasonic bath. Whereas the H₂O-fraction did not contain measurable amounts of the REE, about 80% of the REE budget of LAP 02205 was transferred to the HCl-leachate. Considering the weight loss during leaching we calculate a concentration of 190-270 ppm Nd in the leached phase. This is consistent with phosphate, which has been shown to constitute about 0.3 vol% of LAP 02205 (3). All rock powders were dissolved in HF-HNO₃ for 3 days at 120°C using sealed PFA Savillex beakers. After taking the samples to dryness, the residue was repeatedly treated with small amounts of concentrated HNO₃ to break down insoluble fluoride complexes. The samples were finally taken up in 6N HCl, which produced a clear solution for all samples except Allende, which left an insoluble

carbonaceous residue. Approximately 5% of the sample solutions were removed and spiked with a mixed ^{149}Sm - ^{150}Nd tracer in order to measure Sm and Nd concentrations by isotope dilution (ID). After spiking, the mixed solution was taken to dryness and redissolved in HNO_3 to ensure sample-spike isotope equilibration.

Rare Earth Elements (REE) were first separated as a group in conventional cation exchange columns following the procedures outlined by (4). The REE fractions were then loaded on Eichrom Ln-spec® resin in order to separate neodymium and samarium fractions. The utilized reverse chromatography method may leave traces of the first eluting lighter REE in the subsequently eluting heavier REE fractions. This may result in unwanted interferences during mass spectrometry. To remove the ^{142}Ce interference on ^{142}Nd , a liquid extraction technique (5) was applied on the neodymium cuts. The processed neodymium fractions were then passed through 0.5 ml cation columns to remove sodium introduced from NaBrO_3 used in the Ce extraction procedure. The Nd fractions were finally purified a second time on the Ln-spec columns to improve signal stability during TIMS measurements and dried down with a drop of dilute phosphoric acid. Total procedural blanks for Sm IC, ID and Nd ID measurements ranged between 2-4 and 12-16 pg, respectively, and have been accounted for in the calculation of concentrations. The corrections were always smaller than 0.7%. Blank contributions to Nd IC measurements ranged from 41-94 pg but were negligible compared to >600 ng of processed Nd.

Mass spectrometry

For neodymium isotope measurements, approximately 600 ng of neodymium were loaded with phosphoric acid on degassed double rhenium filaments and measured as Nd^+ -ions on a Finnigan Triton® thermal ionization mass spectrometer at the Johnson Space Center in Houston, Texas. The spectrometer is equipped with 9 faraday cups which allows for the simultaneous

determination of all neodymium isotopes and the two possible interfering elements cerium and samarium, monitored by ^{140}Ce and ^{147}Sm , respectively. The electron deflection magnet located above the z-deflection plates of the Triton focusing system was removed from the ion source and measurements were carried out in static mode. Samples and standards were run at ^{142}Nd beam currents of 4 to $8 \times 10^{-11}\text{A}$.

A typical measurement consisted of 18 or 27 blocks with 20 cycles of 16 second beam integrations using amplifier rotation each block. Baselines were measured before each block with defocused beam as 30 cycles of 1 second integrations. Nd isotope ratios were corrected for instrumental mass fractionation by normalizing each cycle to $^{144}\text{Nd}/^{146}\text{Nd} = 0.7219$ using an exponential law. Repeated measurements of the La Jolla and AMES 97 Nd isotope standards gave average $^{143}\text{Nd}/^{144}\text{Nd}$ of 0.511844 ± 0.000002 (2σ , $n=13$) and 0.512132 ± 0.000002 (2σ , $n=9$), respectively (Table S1, Fig. S1). The $^{142}\text{Nd}/^{144}\text{Nd}$, $^{145}\text{Nd}/^{144}\text{Nd}$, $^{148}\text{Nd}/^{144}\text{Nd}$ and $^{150}\text{Nd}/^{144}\text{Nd}$ ratios are identical within error for the two standards and average 1.141832 ± 0.000006 , 0.348400 ± 0.000002 , 0.241581 ± 0.000004 , and 0.236453 ± 0.000007 (2σ , $n=22$), respectively.

Table S1: Results from Nd isotope analyses of samples and standards by TIMS

Standards	¹⁴² Nd/ ¹⁴⁴ Nd	2σ	¹⁴³ Nd/ ¹⁴⁴ Nd	2σ	¹⁴⁵ Nd/ ¹⁴⁴ Nd	2σ	¹⁴⁸ Nd/ ¹⁴⁴ Nd	2σ	¹⁵⁰ Nd/ ¹⁴⁴ Nd	2σ	Ce corr ppm
Ames 97	1.141830	3.2E-06	0.512132	1.3E-06	0.348401	7.8E-07	0.241579	9.0E-07	0.236448	1.2E-06	0.0
Ames 97	1.141836	3.4E-06	0.512133	1.2E-06	0.348401	6.7E-07	0.241580	9.0E-07	0.236453	1.2E-06	0.0
Ames 97	1.141834	3.1E-06	0.512133	1.3E-06	0.348402	7.4E-07	0.241581	8.6E-07	0.236453	1.2E-06	0.1
Ames 97	1.141829	3.6E-06	0.512133	1.3E-06	0.348401	8.6E-07	0.241580	9.6E-07	0.236451	1.3E-06	0.1
La Jolla	1.141834	4.1E-06	0.511845	1.5E-06	0.348401	8.7E-07	0.241582	1.1E-06	0.236457	1.6E-06	0.1
La Jolla	1.141833	4.1E-06	0.511844	1.5E-06	0.348399	9.3E-07	0.241583	1.0E-06	0.236460	1.6E-06	0.6
La Jolla	1.141832	4.3E-06	0.511846	1.7E-06	0.348402	1.1E-06	0.241581	1.4E-06	0.236454	1.8E-06	1.5
La Jolla	1.141836	4.1E-06	0.511845	1.7E-06	0.348400	1.1E-06	0.241586	1.2E-06	0.236460	1.5E-06	0.8
La Jolla	1.141833	3.2E-06	0.511844	1.1E-06	0.348400	6.8E-07	0.241583	9.1E-07	0.236455	1.2E-06	1.5
La Jolla	1.141835	3.0E-06	0.511843	1.1E-06	0.348400	7.4E-07	0.241584	8.2E-07	0.236456	1.2E-06	0.8
Ames 97	1.141831	4.6E-06	0.512130	1.8E-06	0.348399	1.1E-06	0.241578	1.2E-06	0.236449	1.7E-06	0.8
La Jolla	1.141834	4.4E-06	0.511842	1.8E-06	0.348401	9.8E-07	0.241580	1.2E-06	0.236454	1.7E-06	0.0
La Jolla	1.141833	3.9E-06	0.511845	1.5E-06	0.348401	8.1E-07	0.241582	1.0E-06	0.236453	1.5E-06	3.3
La Jolla	1.141836	3.5E-06	0.511844	1.3E-06	0.348399	8.2E-07	0.241581	9.1E-07	0.236454	1.3E-06	1.8
Ames 97	1.141828	3.7E-06	0.512132	1.4E-06	0.348399	8.5E-07	0.241580	9.7E-07	0.236449	1.3E-06	1.5
Ames 97	1.141832	5.3E-06	0.512131	2.0E-06	0.348400	1.3E-06	0.241580	1.4E-06	0.236448	1.9E-06	2.7
La Jolla	1.141838	2.9E-06	0.511845	1.2E-06	0.348399	6.6E-07	0.241583	8.2E-07	0.236456	1.1E-06	1.8
Ames 97	1.141833	3.4E-06	0.512131	1.3E-06	0.348400	7.5E-07	0.241580	9.7E-07	0.236453	1.3E-06	1.4
Ames 97	1.141830	4.0E-06	0.512131	1.7E-06	0.348400	1.0E-06	0.241579	1.3E-06	0.236450	1.6E-06	2.8
La Jolla	1.141827	3.1E-06	0.511843	1.2E-06	0.348399	6.7E-07	0.241580	8.7E-07	0.236450	1.1E-06	3.8
La Jolla	1.141829	3.7E-06	0.511845	1.3E-06	0.348401	8.3E-07	0.241579	1.1E-06	0.236448	1.4E-06	1.5
La Jolla	1.141830	3.8E-06	0.511844	1.4E-06	0.348401	8.1E-07	0.241580	1.0E-06	0.236453	1.4E-06	1.7
AMES mean	1.141831		0.512132		0.348400		0.241580		0.236450		1.0
2σ ±	0.000005		0.000002		0.000002		0.000002		0.000004		2.2
LJ mean	1.141833		0.511844		0.348400		0.241582		0.236455		1.5
2σ ±	0.000006		0.000002		0.000002		0.000004		0.000007		2.2
mean all	1.141832				0.348400		0.241581		0.236453		1.3
2σ ±	0.000006				0.000002		0.000004		0.000007		2.2
.218 Ames	1.141859	3.7E-06	0.512132	1.4E-06	0.348401	7.9E-07	0.241582	9.1E-07	0.236453	1.3E-06	1.9
.218 Ames	1.141859	3.4E-06	0.512132	1.3E-06	0.348400	8.8E-07	0.241580	1.1E-06	0.236450	1.3E-06	0.7
.218 Ames	1.141856	3.6E-06	0.512133	1.5E-06	0.348400	7.9E-07	0.241581	8.9E-07	0.236453	1.2E-06	0.5
mean	1.141858		0.512132		0.348400		0.241581		0.236452		1.0
2σ ±	0.000003		0.000001		0.000001		0.000003		0.000003		1.4
.430 Ames	1.141884	3.6E-06	0.512132	1.4E-06	0.348400	8.8E-07	0.241581	1.1E-06	0.236453	1.4E-06	2.3
.430 Ames	1.141885	3.6E-06	0.512132	1.2E-06	0.348400	7.5E-07	0.241580	9.0E-07	0.236456	1.3E-06	1.4
.430 Ames	1.141888	3.6E-06	0.512133	1.4E-06	0.348400	8.6E-07	0.241581	9.8E-07	0.236456	1.3E-06	1.4
mean	1.141885		0.512133		0.348400		0.241581		0.236455		1.7
2σ ±	0.000004		0.000001		0.000001		0.000001		0.000003		1.1
.638 Ames	1.141899	4.1E-06	0.512131	1.5E-06	0.348400	9.0E-07	0.241581	1.1E-06	0.236452	1.4E-06	3.1
.638 Ames	1.141905	3.9E-06	0.512135	1.4E-06	0.348401	8.2E-07	0.241581	1.1E-06	0.236452	1.4E-06	1.3
.638 Ames	1.141907	2.4E-06	0.512132	9.5E-07	0.348400	6.0E-07	0.241581	7.2E-07	0.236453	9.5E-07	0.6
mean	1.141904		0.512133		0.348400		0.241581		0.236452		1.7
2σ ±	0.000009		0.000004		0.000002		0.000000		0.000001		2.6
Samples											
LAP WR A	1.141814	5.5E-06	0.514171	2.0E-06	0.348398	1.2E-06	0.241579	1.5E-06	0.236447	2.0E-06	0.4
LAP WR B	1.141810	4.4E-06	0.514116	1.6E-06	0.348399	1.1E-06	0.241577	1.2E-06	0.236447	1.6E-06	0.3
LAP WR A-L	1.141812	2.9E-06	0.512166	1.1E-06	0.348399	6.7E-07	0.241579	8.1E-07	0.236459	1.1E-06	0.5
LAP WR B-L	1.141813	4.1E-06	0.512176	1.6E-06	0.348400	9.3E-07	0.241580	1.1E-06	0.236460	1.6E-06	5.6
LAP WR B-L	1.141809	3.4E-06	0.512174	1.3E-06	0.348398	8.6E-07	0.241578	9.2E-07	0.236455	1.3E-06	1.2
LAP WR C*	1.141814	3.3E-06	0.512670	1.3E-06	0.348399	7.7E-07	0.241578	9.5E-07	0.236446	1.2E-06	1.0
LAP WR D-L	1.141814	3.2E-06	0.512147	1.2E-06	0.348399	7.3E-07	0.241579	8.9E-07	0.236451	1.2E-06	1.0
mean	1.141812				0.348399		0.241578		0.236452		1.4
2σ ±	0.000004				0.000001		0.000002		0.000012		3.8
SaU 169	1.141795	3.3E-06	0.511791	1.2E-06	0.348397	7.5E-07	0.241579	8.9E-07	0.236449	1.3E-06	1.1
SaU 169	1.141796	3.0E-06	0.511792	1.4E-06	0.348397	8.5E-07	0.241578	9.6E-07	0.236449	1.2E-06	1.2
mean	1.141795		0.511792		0.348397		0.241578		0.236449		1.2
2σ ±	0.000006		0.000002		0.000001		0.000000		0.000002		0.2
15386	1.141790	3.4E-06	0.511798	1.3E-06	0.348394	7.7E-07	0.241580	9.2E-07	0.236453	1.2E-06	4.2
15386-2	1.141795	3.2E-06	0.511798	1.2E-06	0.348395	7.8E-07	0.241579	8.8E-07	0.236450	1.3E-06	3.0
15386	1.141795	3.2E-06	0.511801	1.2E-06	0.348395	8.2E-07	0.241578	8.5E-07	0.236452	1.3E-06	1.9
mean	1.141794		0.511799		0.348395		0.241579		0.236451		3.0
2σ ±	0.000006		0.000003		0.000001		0.000002		0.000003		2.3
74275	1.141839	2.7E-06	0.514178	1.1E-06	0.348400	6.6E-07	0.241580	7.6E-07	0.236449	1.0E-06	0.6
70017	1.141834	2.9E-06	0.514720	1.1E-06	0.348400	6.9E-07	0.241577	8.2E-07	0.236445	1.1E-06	0.7
15555	1.141814	5.3E-06	0.512879	1.8E-06	0.348399	1.3E-06	0.241583	1.5E-06	0.236475	2.1E-06	1.8
Allende	1.141785	4.1E-06	0.512590	1.5E-06	0.348401	9.9E-07	0.241582	1.1E-06	0.236481	1.7E-06	2.2

*unleached

Table S1 cont.

Standards	$\epsilon^{142}\text{Nd}$	$\epsilon^{143}\text{Nd}$	$\epsilon^{145}\text{Nd}$	$\epsilon^{148}\text{Nd}$	$\epsilon^{150}\text{Nd}$	$\epsilon^{144}\text{Sm}$	$\epsilon^{148}\text{Sm}$	$\epsilon^{149}\text{Sm}$	$\epsilon^{150}\text{Sm}$	$\epsilon^{152}\text{Sm}$
Ames 97	-0.02	-9.85	0.01	-0.08	-0.22					
Ames 97	0.03	-9.82	0.03	-0.04	0.01					
Ames 97	0.02	-9.83	0.04	0.01	0.00					
Ames 97	-0.03	-9.84	0.02	-0.04	-0.08					
La Jolla	0.01	-15.45	0.01	0.05	0.19					
La Jolla	0.00	-15.47	-0.03	0.07	0.28					
La Jolla	0.00	-15.44	0.05	0.02	0.05					
La Jolla	0.03	-15.45	-0.01	0.19	0.30					
La Jolla	0.01	-15.47	-0.02	0.09	0.09					
La Jolla	0.02	-15.48	0.00	0.11	0.14					
Ames 97	-0.01	-9.89	-0.04	-0.11	-0.15					
La Jolla	0.01	-15.50	0.01	-0.03	0.03					
La Jolla	0.01	-15.45	0.02	0.03	0.01					
La Jolla	0.03	-15.47	-0.04	0.01	0.04					
Ames 97	-0.04	-9.85	-0.03	-0.04	-0.15					
Ames 97	-0.01	-9.87	0.00	-0.06	-0.22					
La Jolla	0.05	-15.44	-0.03	0.10	0.12					
Ames 97	0.01	-9.87	-0.01	-0.05	0.00					
Ames 97	-0.02	-9.87	0.00	-0.09	-0.12					
La Jolla	-0.05	-15.49	-0.03	-0.05	-0.11					
La Jolla	-0.03	-15.45	0.01	-0.07	-0.19					
La Jolla	-0.02	-15.48	0.02	-0.02	0.00					
AMES mean	-0.01		0.00	-0.06	-0.10					
2 σ \pm	0.04		0.05	0.07	0.18					
LJ mean	0.01		0.00	0.04	0.07					
2 σ \pm	0.05		0.05	0.15	0.28					
mean all	0.00		0.00	0.00	0.00					
2 σ \pm	0.05		0.05	0.15	0.30					
.218 Ames	0.23	-9.85	0.02	0.06	-0.02					
.218 Ames	0.23	-9.84	0.00	-0.05	-0.11					
.218 Ames	0.21	-9.83	-0.01	0.01	0.00					
mean	0.23	-9.84	0.00	0.01	-0.04					
2 σ \pm	0.03	0.02	0.03	0.12	0.12					
.430 Ames	0.45	-9.84	0.00	0.01	0.01					
.430 Ames	0.46	-9.84	-0.01	-0.03	0.12					
.430 Ames	0.48	-9.83	-0.01	0.02	0.12					
mean	0.46	-9.84	-0.01	0.00	0.08					
2 σ \pm	0.03	0.01	0.02	0.06	0.12					
.638 Ames	0.58	-9.87	-0.02	0.00	-0.05					
.638 Ames	0.64	-9.79	0.02	0.00	-0.04					
.638 Ames	0.65	-9.86	-0.01	0.02	0.00					
mean	0.62	-9.84	0.00	0.01	-0.03					
2 σ \pm	0.08	0.09	0.04	0.02	0.05					
Samples										
LAP WR A	-0.16	29.92	-0.06	-0.09	-0.27	-0.93	0.46	-3.37	7.10	0.32
LAP WR B	-0.20	28.85	-0.03	-0.15	-0.25	0.40	-0.11	-3.57	6.62	0.20
LAP WR A-L	-0.18	-9.18	-0.03	-0.09	0.26	-0.18	-0.06	-3.50	6.35	-0.04
LAP WR B-L	-0.17	-8.99	-0.01	-0.04	0.30	0.63	0.19	-3.30	6.81	0.06
LAP WR B-L	-0.20	-9.03	-0.05	-0.14	0.07	-0.42	-0.22	-3.62	6.09	-0.09
LAP WR C	-0.16	0.65	-0.05	-0.14	-0.29	0.01	0.07	-3.43	6.35	0.09
LAP WR D-L	-0.16	-9.57	-0.03	-0.09	-0.08	-0.11	-0.10	-3.48	5.92	-0.04
mean	-0.18	0.65	-0.04	-0.11	-0.04	-0.09	0.04	-3.47	6.46	0.07
2 σ \pm	0.04		0.04	0.07	0.50	1.03	0.46	0.22	0.82	0.29
SAU 169	-0.32	-16.51	-0.11	-0.10	-0.15					
SAU 169	-0.31	-16.48	-0.09	-0.11	-0.17					
mean	-0.32	-16.48	-0.10	-0.11	-0.18	-0.28	0.01	-12.48	22.54	-0.57
2 σ \pm	0.05	0.05	0.02	0.02	0.07					
15386	-0.37	-16.37	-0.17	-0.04	-0.01					
15386-2	-0.33	-16.37	-0.16	-0.09	-0.14					
15386	-0.32	-16.32	-0.16	-0.11	-0.04					
mean	-0.34	-16.35	-0.17	-0.08	-0.06	-0.34	0.18	-32.51	60.07	-0.91
2 σ \pm	0.05	0.06	0.02	0.08	0.13					
74275	0.06	30.06	-0.01	-0.06	-0.16	-0.60	-0.17	-1.88	3.16	-0.03
70017	0.01	40.64	-0.01	-0.15	-0.33	-1.33	-0.25	-1.37	2.59	0.15
15555	-0.16	4.71	-0.04	0.07	0.93	-0.50	0.06	-5.28	10.30	0.28
Allende	-0.41	-0.91	0.03	0.06	1.18	-5.25	-1.01	-0.59	-1.85	-0.19

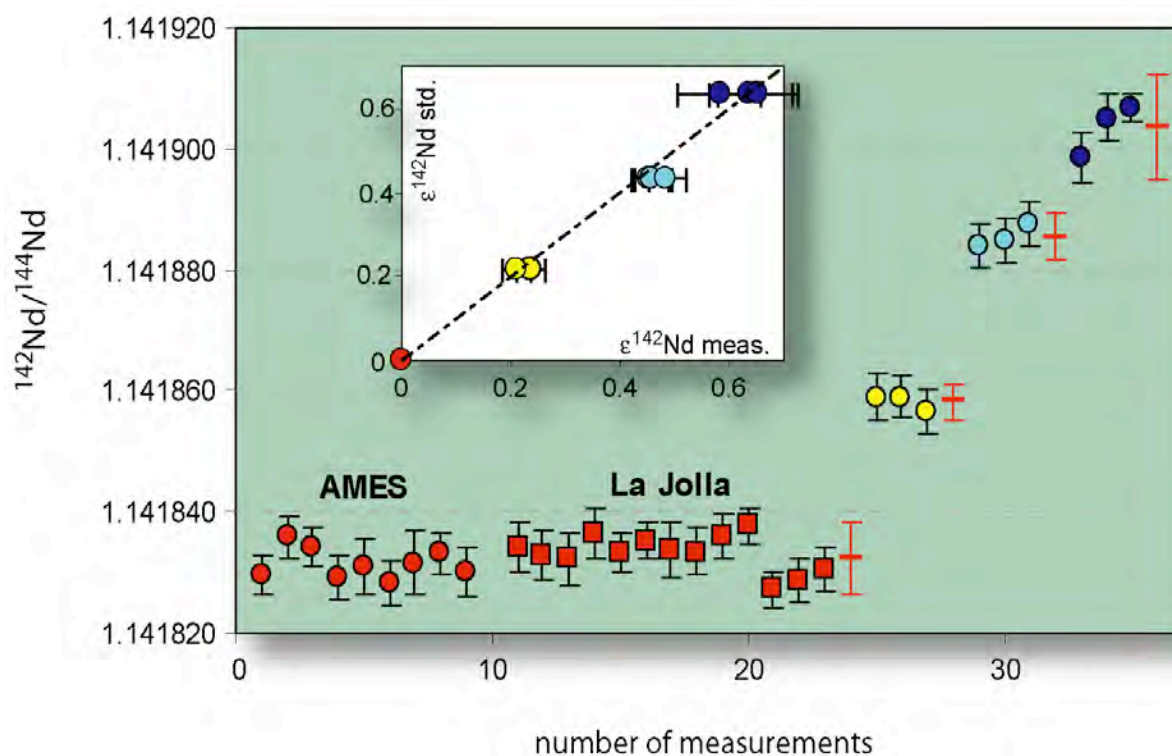


Figure S1: Reproducibility of $^{142}\text{Nd}/^{144}\text{Nd}$ ratios of terrestrial standards AMES 97 and La Jolla (red dots and squares) and enriched standards AMES 0.218 (yellow), AMES 0.430 (light blue) and AMES 0.638 (blue) during the period of analyses along with their averages and 2σ -errors (red bars). The inset shows measured vs. enriched standard $\epsilon^{142}\text{Nd}$. The slope of the regression line is 1.01 ($R^2 = 0.97$). Long-term (March to November 2005) external reproducibility of $\epsilon^{142}\text{Nd}$ for all 22 standards is ± 5.3 ppm (2σ). Except for one run of the 0.638 standard which gave a slightly low value, the reproducibility of the enriched standards is smaller or equal to that of the terrestrial standards.

A recent investigation reported correlated $^{142}\text{Nd}/^{144}\text{Nd}$ and $^{150}\text{Nd}/^{144}\text{Nd}$ ratios in exponential law normalized measurements when the electron deflection magnet was not removed from the Triton ion source (6). Although the magnet was removed for all measurements, a weak correlation (MSWD=1.5; $p=0.058$) is observed for measured $^{142}\text{Nd}/^{144}\text{Nd}$ - $^{150}\text{Nd}/^{144}\text{Nd}$ ratios (Fig. S2). This might be related to some residual cup bias for the static measurement mode employed in these measurements, as opposed to the time-consuming multidynamic measurements of (6).

However, no second-order correction is applied to the data in Table S1, as was done by (7), because the ultimate origin of the relationship remains unclear.

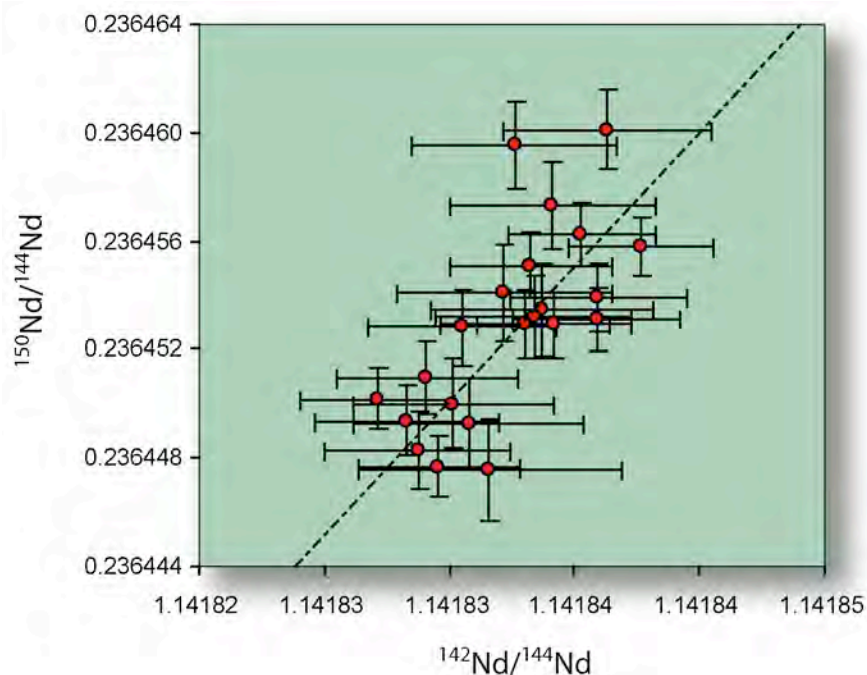


Figure S2: $^{142}\text{Nd}/^{144}\text{Nd}$ vs. $^{150}\text{Nd}/^{144}\text{Nd}$ in all analyzed standards.

Five high intensity measurements of a Sm standard solution produced mean $^{144}\text{Sm}/^{152}\text{Sm}$, $^{148}\text{Sm}/^{152}\text{Sm}$, $^{149}\text{Sm}/^{152}\text{Sm}$, $^{150}\text{Sm}/^{152}\text{Sm}$ and $^{154}\text{Sm}/^{152}\text{Sm}$ ratios of 0.114985 ± 0.000006 , 0.420454 ± 0.000007 , 0.516864 ± 0.000009 , 0.275997 ± 0.000003 and 0.850781 ± 0.000013 (normalized to $^{147}\text{Sm}/^{152}\text{Sm} = 0.560828$; all errors are 2σ). The results are in agreement with the values reported by (8).

The utilized chemistry resulted in very pure neodymium fractions with undetectable ^{147}Sm , and corrections on $^{142}\text{Nd}/^{144}\text{Nd}$ ratios from ^{142}Ce interference were always lower than 6 ppm, but mostly below 1 ppm (cf. Table S1). There is no correlation between the Ce correction and measured $^{142}\text{Nd}/^{144}\text{Nd}$ ratios in 7 duplicate determinations of LAP 02205 (Fig. S3).

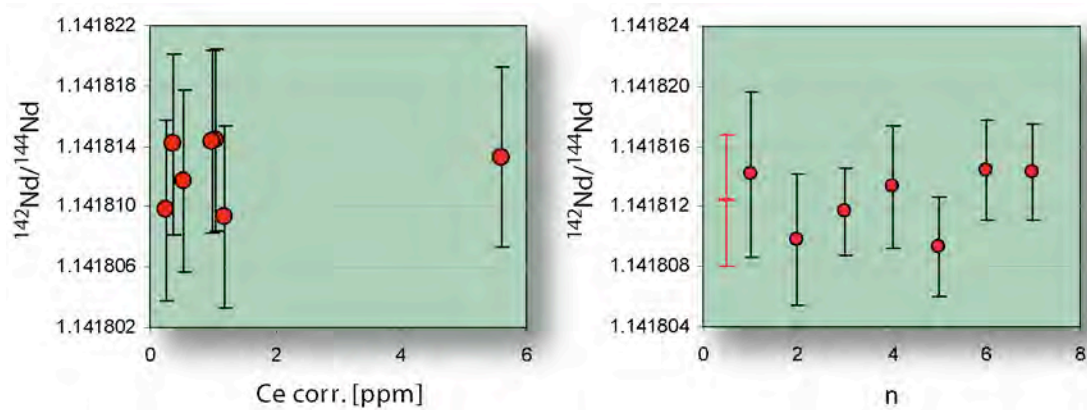


Figure S3 (left): Ce correction vs. $^{142}\text{Nd}/^{144}\text{Nd}$ of duplicated sample LAP 02205. There is no observable trend, confirming that interferences from ^{142}Ce are properly corrected for and do not affect the measured values.

Figure S4 (right): Reproducibility of $^{142}\text{Nd}/^{144}\text{Nd}$ ratios of sample LAP 02205. Individual points refer to different sample dissolutions and chemistries. External reproducibility was 1.1418124 ± 0.0000043 (2σ).

Moreover, the external precision on all Nd isotope ratios calculated from duplicate determinations of samples LAP 02205 (6 separate dissolutions), SaU 169 ($n=3$) and KREEP basalt 15386 ($n=3$) is similar to the precision reported for the standard (Table S1, Fig. S4). This confirms that interferences from Sm or Ce do not bias the results reported in Table S1, and that determination of sample $^{142}\text{Nd}/^{144}\text{Nd}$ was both precise and accurate within the ± 5.3 ppm (2σ) external precision based on replicate measurements of the standards. All sample Nd and Sm isotope determinations in Table S1 are also reported in ϵ -notation (9) relative to the measured standards. However, $\epsilon^{143}\text{Nd}$ and $\epsilon^{143}\text{Nd}_{\text{ini}}$ were calculated by normalizing to the value for the chondritic uniform reservoir (CHUR). CHUR has recently been redetermined to $^{143}\text{Nd}/^{144}\text{Nd}_{\text{CHUR, today}} = 0.512637$ and $^{147}\text{Sm}/^{144}\text{Nd}_{\text{today}} = 0.1964$ (10). The $\epsilon^{142}\text{Nd}_{\text{ini}}$ value at the time of sample crystallization has been calculated using the measured Sm/Nd ratio, $^{146}\text{Sm}/^{144}\text{Sm} = 0.0075$ (10), $^{144}\text{Sm}/^{147}\text{Sm} = 0.205027$ (mean of 7 Sm std measurements) and $\lambda^{146}\text{Sm} = 6.74 \times 10^{-9} \text{ yrs}^{-1}$.

Neodymium concentrations were determined on the Triton in 9 blocks with 10 cycles of 8 seconds integration time and identical cup configuration as Nd IC-runs. An offline iterative spike stripping procedure was applied to each scan of the measured raw data, resulting in precise concentration data and independent determinations of the $^{142}\text{Nd}/^{144}\text{Nd}$, $^{143}\text{Nd}/^{144}\text{Nd}$, $^{145}\text{Nd}/^{144}\text{Nd}$ and $^{148}\text{Nd}/^{144}\text{Nd}$ ratios to check for inconsistencies with IC measurements. For the calculation of Sm concentrations, accurate sample Sm isotopic compositions were obtained from contemporaneous unspiked runs and included in the spike stripping algorithm. Interferences on masses ^{144}Sm , ^{148}Sm and ^{150}Sm from ^{144}Nd , ^{148}Nd and ^{150}Nd were corrected for by monitoring ^{143}Nd and using the appropriate $^{143}\text{Nd}/^{144}\text{Nd}$, $^{143}\text{Nd}/^{148}\text{Nd}$ and $^{143}\text{Nd}/^{150}\text{Nd}$ ratios of each sample. Application of individual corrections for the calculation of Sm concentrations led to significant improvements of the Sm/Nd reproducibility. Because use of a mixed Sm/Nd spike cancels out errors introduced from sample/spike weighing, the accuracy of the measured Sm/Nd ratio is mainly delimited by the spike calibration itself which was set to a fixed value of 0.1%.

To test for the accuracy of our Sm/Nd spike calibration, we analyzed three additional splits of the Allende CV3 chondrite for Sm/Nd concentrations and $^{143}\text{Nd}/^{144}\text{Nd}$ isotope composition along with an aliquot of the CIT n(Sm/Nd) β standard ($^{147}\text{Sm}/^{144}\text{Nd} = 0.19655$ (11)). The results for Allende are presented in Table S2 and Figure S5 and compared to Allende analyses from the literature (10-12).

	Mass [mg]	[Sm]	[Nd]	$^{147}\text{Sm}/^{144}\text{Nd}$	$^{143}\text{Nd}/^{144}\text{Nd}$
CIT n(Sm/Nd) β		57.21 ± 0.05 ng	176.01 ± 0.05 ng	0.1965 ± 0.0002	0.511899
Allende 1a rock chip	53.45	0.2943 ppm	0.9725 ppm	0.1830	0.512210
Allende 1b rock chip	89.90	0.2953 ppm	0.9762 ppm	0.1829	0.512212
Allende 2 homog. powder	22.45	0.2935 ppm	0.9143 ppm	0.1941	0.512595

Table S2: Results from replicate Sm-Nd analyses of the Allende chondrite.

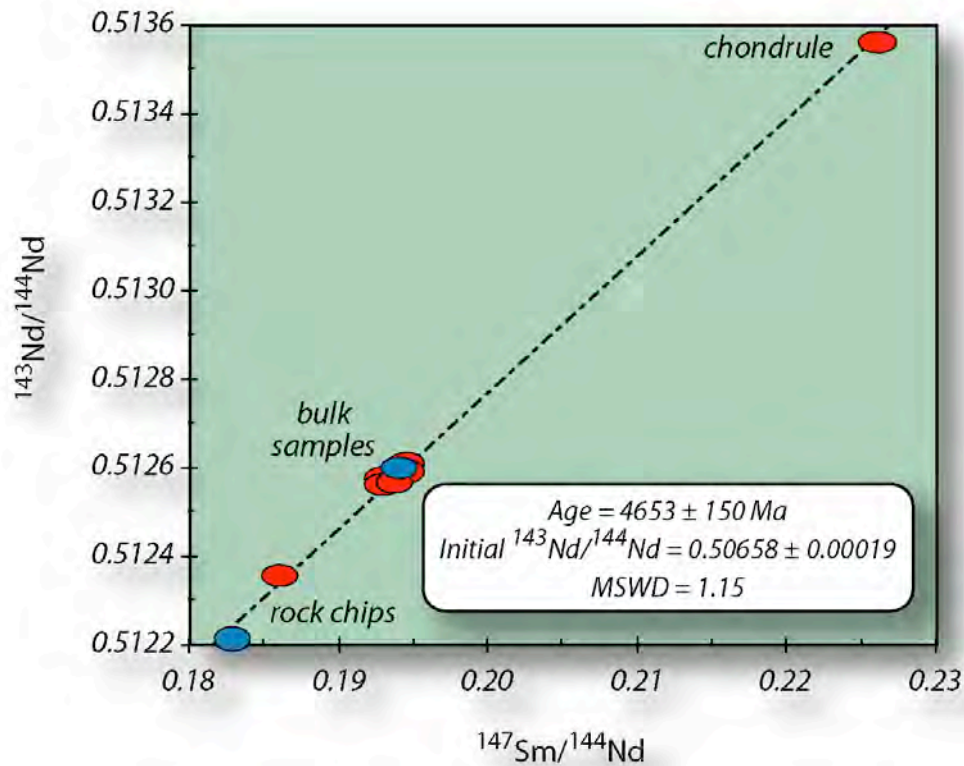


Figure S5: Results from Sm/Nd isotope determinations of three aliquots (blue) of the Allende chondrite along with other literature data (10-12) for the same sample. Taken together, all 10 aliquots plot along an isochron which is consistent with the accepted age of 4.567 Ga (10) for Allende. Homogenized bulk rocks cluster at $^{147}\text{Sm}/^{144}\text{Nd} \sim 0.1940$ and $^{143}\text{Nd}/^{144}\text{Nd} \sim 0.51258$. The chondrule separate defines the most unradiogenic composition. Smaller fragments (chips) of Allende display considerable heterogeneity, although two determinations from the same small chip (~100 mg) are indistinguishable in composition (lower left).

There are three important conclusions emerging from these data: a) Taken together, all 10 aliquots plot along an isochron which is consistent with the accepted age of 4567 m.y. (10) for Allende. This is consistent with our measured $^{147}\text{Sm}/^{144}\text{Nd}$ ratios being comparable to the results of other labs. b) If small fragments of Allende are analyzed (excluding the chondrule separate), $^{147}\text{Sm}/^{144}\text{Nd}$ ratios may vary from 0.1829 to 0.1946, corresponding to correlated present-day $\epsilon^{143}\text{Nd}$ of -8.3 to -0.6 and predicted $\epsilon^{142}\text{Nd}$ -0.35 to -0.22. Sample heterogeneity thus is mani-

fested in the mm (rock chip) scale, because the two replicates of the same ~100mg powdered rock chip have indistinguishable Sm/Nd composition (Table S2). If a chondrule fragment is included in the analyses, $\epsilon^{142}\text{Nd}$ may even be positive, and explain the preliminary data presented in (13). However, this should be evident from correlated high $\epsilon^{143}\text{Nd}$, which was not given in the cited abstract. c) Whenever larger, homogenized samples are analyzed, the Allende data are very reproducible, have $^{147}\text{Sm}/^{144}\text{Nd} \sim 0.1941$ and $\epsilon^{143}\text{Nd} \sim -1$.

Neutron capture effects on samarium isotopes

In a thin planetary atmosphere, neutrons are generated by nuclear interactions between high energy galactic cosmic rays (87% protons with energies of 0.1 to 10 GeV) and the nuclei of the surface material. After production (most with energies above a few MeV), neutrons exchange energy with regolith material and eventually come to equilibrium (14). Rocks exposed at the lunar surface may therefore show alterations in their initial isotopic composition because of neutron capture (15). Sensitive monitors for such process are nuclides with large thermal neutron absorption cross sections such as ^{149}Sm or ^{157}Gd . These capture reactions cause anomalous decreases in the abundance of the target nuclei ^in and anomalous increases in the abundance of the product nuclei ^{i+1}n . If a suite of samples was exposed to different neutron doses they should thus form correlations with slope -1 on binary plots of e.g. $^{149}\text{Sm}/^{152}\text{Sm}$ vs. $^{150}\text{Sm}/^{152}\text{Sm}$. Figure S6 shows results from Sm isotope analyses of lunar samples analyzed in this study, normalized to $^{147}\text{Sm}/^{152}\text{Sm}=0.560828$. Calculated $\epsilon^{149}\text{Sm}=(^{149}\text{Sm}/^{152}\text{Sm})_{\text{meas}}/(^{149}\text{Sm}/^{152}\text{Sm})_{\text{Std}}-1)*10000$ ranges from -0.35 in Allende to -32.1 in sample 15386 (Table S1). A similar high value of -31.6 ± 0.5 for sample 15386 has been found by Nyquist et al. (16). The regressed line has a slope of -1.01 ± 0.02 , consistent with the assumption that the observed isotopic variation is caused by neutron capture. However, the nuclide ^{152}Sm which is used for normalization may also be both eroded

($^{152}\text{Sm}(n,\gamma)^{153}\text{Sm}(\beta^-)^{153}\text{Eu}$; $\sigma_a=206$ barns) and produced by neutron capture ($^{151}\text{Eu}(n,\gamma)^{152}\text{Eu}(\beta^+)^{152}\text{Sm}$; 9164 barns, $p=72.1\%$), giving rise to possible misinterpretations of the normalized data. One way to investigate this problem is to normalize the measured raw data to $^{147}\text{Sm}/^{154}\text{Sm} = 0.65918$. ^{154}Sm has a small neutron capture cross section (8.4 barns) and is only minimally produced by the reaction $^{153}\text{Eu}(n,\gamma)^{154}\text{Eu}(\beta^+)^{154}\text{Sm}$ (313 barns, $p=0.02\%$). ^{147}Sm also has a small cross section (57 barns) and its production via $^{146}\text{Nd}(n,\gamma)^{147}\text{Nd}(\beta^-)^{147}\text{Pm}(\beta^-)^{147}\text{Sm}$ (1.4 barns) is negligible. The $^{147}\text{Sm}/^{154}\text{Sm}$ ratio should therefore provide a reliable basis for normalization. Normalizing the data to $^{147}\text{Sm}/^{154}\text{Sm}$ yields a slope of -0.98 ± 0.02 in $^{149}\text{Sm}/^{154}\text{Sm}$ vs. $^{150}\text{Sm}/^{154}\text{Sm}$ isotope space, which is within error identical to that obtained from the $^{147}\text{Sm}/^{152}\text{Sm}$ normalization procedure (Fig. S7). Hence, we conclude that neutron capture caused the observed Sm isotopic variation.

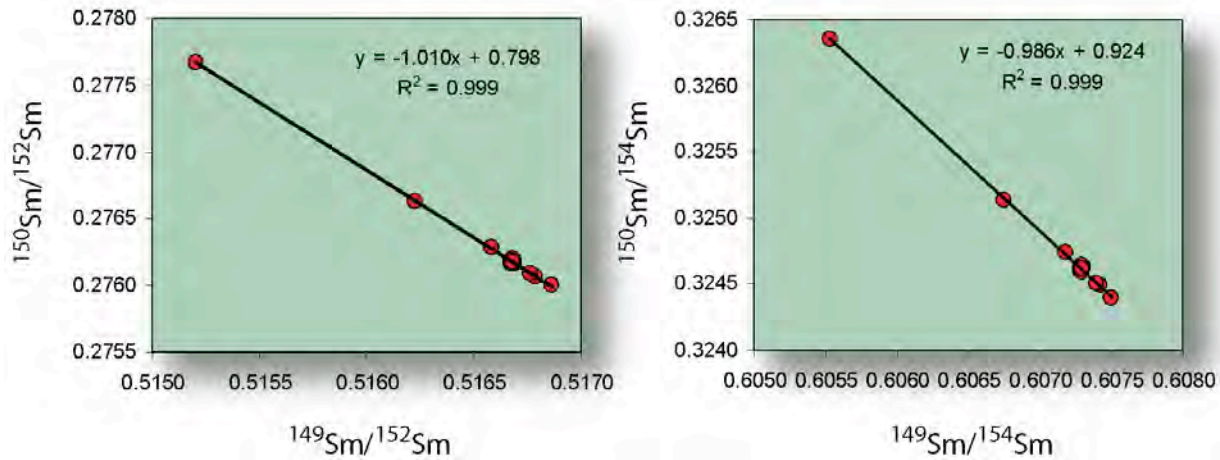


Figure S6 and S7: Results from Sm isotope measurements normalized to $^{147}\text{Sm}/^{152}\text{Sm}$ (left) and $^{147}\text{Sm}/^{154}\text{Sm}$ (right). 2σ -errors are smaller than symbol size. The terrestrial standard is defined by the point in the lower right. Increasing exposure to neutron irradiation shifts the value to the upper left. Lunar samples conform to the theoretical prediction of a slope -1 for neutron capture.

Calculated $\epsilon^{149}\text{Sm}$ for irradiated lunar samples differ by less than 5% for the two normalization schemes and are in close agreement with previous data (16). However, because the

$^{147}\text{Sm}/^{154}\text{Sm}$ fractionation correction is robust against effects from ^{151}Eu (except $\epsilon^{152}\text{Sm}$), these data are reported in Table S1 and are used for the calculation of the thermal neutron fluence in each individual sample. The external precision on sample samarium isotope ratios was smaller than ± 22 ppm for both schemes except $\epsilon^{144}\text{Sm}$ (~ 100 ppm), which is attributed to the greater impact of the ^{144}Nd interference on the low-abundant ^{144}Sm .

Correction on neodymium isotope compositions

By far the largest effect of thermal neutron irradiation on neodymium is the reaction $^{143}\text{Nd}(n,\gamma)^{144}\text{Nd}$ with a capture cross section of 336 barns. This affects the $^{143}\text{Nd}/^{144}\text{Nd}$ ratio directly, but also the $^{142}\text{Nd}/^{144}\text{Nd}$ and $^{143}\text{Nd}/^{144}\text{Nd}$ ratios indirectly via the $^{146}\text{Nd}/^{144}\text{Nd}$ normalization scheme. Corrections are non-trivial for the two KREEP samples SaU 169 and 15386 in the context of the present study (cf. Table S3) and need to be properly corrected for. However, it is most important to note that the irradiation-induced correction of $\epsilon^{142}\text{Nd}$ is smaller than the analytical precision for the other four lunar samples.

Sample	$\epsilon^{142}\text{Nd}$ $\pm 2\sigma$	$\epsilon^{149}\text{Sm}$	$\epsilon^{142}\text{Nd}$ corr	$\Delta\epsilon$
LAP 02205	-0.18 \pm 0.04	-3.5	-0.15	0.03
SaU 169	-0.32 \pm 0.05	-12.5	-0.26	0.06
15386	-0.34 \pm 0.05	-32.5	-0.19	0.15
74275	0.06 \pm 0.05	-1.9	0.07	0.01
70017	0.01 \pm 0.05	-1.4	0.02	0.01
15555	-0.16 \pm 0.05	-5.3	-0.13	0.03
Allende	-0.41 \pm 0.05	-0.3	-0.41	0

Table S3: Correction on $\epsilon^{142}\text{Nd}$ from measured $\epsilon^{149}\text{Sm}$ data. Only the two KREEP samples (bold red) need corrections greater than the external analytical precision of TIMS measurements (± 0.05).

In a pioneering work, Lingenfelter et al. (17) constructed a theoretical neutron energy spectrum for the Apollo 11 lunar soil in order to calculate capture rates for the nuclides Gd, Sm, Eu, Cd, Ba, W, Br and their relative change in isotopic composition. As long as the resonance energies of the nuclides lie well above thermal energies, neutron capture rates are independent on the shape of the neutron energy profile and the relative isotopic shifts of the isotopes due to neutron irradiation can simply be scaled according to their tabulated thermal neutron absorption cross sections (σ_a). Unfortunately, ^{149}Sm , ^{155}Gd and ^{157}Gd all have resonance energies which lie within the thermal energy regime (0.0973, 0.0268 and 0.0314 eV, respectively), and the shape of the neutron energy spectrum in the sample material thus becomes an important factor for the relative capture rates. Lingenfelter et al. (17) therefore adopted ‘effective’ cross sections (σ_{eff}) for ^{149}Sm , ^{155}Gd and ^{157}Gd . The calculated values for σ_{eff} in their formalism include the effect of epithermal neutrons and the lunar neutron energy spectrum, and vary with the major and trace element composition of the surrounding material (17).

A comprehensive discussion of the effects of neutron irradiation on samarium and neodymium isotopes was given by Nyquist et al. (16). The authors calculate values for the thermal (≤ 0.5 eV) and epithermal (≥ 0.5 eV) neutron flux in lunar samples from the measured isotopic shift $\Delta N_i/N_i$ of the samarium isotopes. These neutron fluences are then conversely used to calculate the isotopic shift of neodymium isotopes in the same samples. This ‘intrinsic’ approach is thus independent of the major/trace element composition of each rock and its environment. A variation of this approach was used to correct for the effects of neutron irradiation in this work and is outlined in detail below.

The equations used for neutron fluence corrections are from Nyquist et al. (16). The absorption cross section data for the thermal energy regime was calculated for average cross sections with a Maxwellian energy distribution at a mean temperature of 20°C. This was done for a

given nuclide, temperature and the thermal energy interval from 0.00001 to 0.5 eV with the JEFF-3.1 nuclear data library (18) using the INTER, LINEAR and RECENT codes (19). (cf. Table S4 with a compilation of all relevant neutron data). For nuclides with a linear dependence of the absorption cross sections on neutron energy (1/v-absorber), there is no difference to the standard 0.0253 eV value. For ^{149}Sm , however, the cross section is a factor of 1.7 higher and accounts for the resonance at 0.0973 eV (the same is true for e.g. ^{113}Cd , ^{151}Eu , $^{155,157}\text{Gd}$, ^{167}Er and ^{176}Lu). Average resonance integrals for the epithermal energy regime (0.5 to 100000 eV with a 1/E energy distribution) were calculated using the same database.

	σ thermal Maxw.av.	1. res. [eV]	σ epi- thermal
$\sigma^{149}\text{Sm}$	71627	0.0973	3486
$\sigma^{141}\text{Pr}$	11.5	85.2	17.9
$\sigma^{142}\text{Nd}$	18.6	218.6	6.1
$\sigma^{143}\text{Nd}$	335	55.3	132
$\sigma^{144}\text{Nd}$	3.6	373.8	4.1
$\sigma^{145}\text{Nd}$	41.9	4.35	231
$\sigma^{146}\text{Nd}$	1.4	359.5	2.7
$\sigma^{148}\text{Nd}$	2.5	94.9	19.7
$\sigma^{150}\text{Nd}$	1.2	78.8	15.6

Table S4: σ_a for the thermal energy range (Maxwellian average for 1e-5 to 0.5 eV, $T = 0.0253$ eV), first resonance energies and epithermal (1/E average, 0.5-1e5 eV) cross sections of the nuclides discussed.

From Table S4 it can be concluded that higher fluences of epithermal (i.e. with energies greater than 0.5 eV) neutrons lead to pronounced negative anomalies in ^{145}Nd , coupled with positive anomalies in the daughter ^{146}Nd . Higher fractions of epithermal neutrons than calculated by Lingenfelter (17) for the lunar soil have been suggested by numerous workers based on comparison of ^{149}Sm and ^{157}Gd anomalies (20, 21), constraints from additional analysis of ^{113}Cd (22), and most notably, on direct measurements in the lunar soil (23). Ratios of thermal to epithermal neu-

trons (Φ/Ξ) calculated by Nyquist (16) range from 0.31 to 3.03, but are afflicted with an uncertainty factor of ~ 2 . However, the higher precision measurements on the Triton TIMS could not reliably determine Sm isotope anomalies except $\Delta^{149}\text{Sm}/^{149}\text{Sm}$ in weak to intermediately irradiated samples. Residual interferences from Nd, Gd and BaO on the samarium isotopes limit the accuracy on $\epsilon^{148}\text{Sm}$ and $\epsilon^{150}\text{Sm}$ to at least 20-30 ppm in the present study. A more sophisticated chemistry might resolve those problems in the future. At present, however, Φ/Ξ ratios cannot be determined from Sm isotopes to the desired accuracy in the percent range even for the most heavily irradiated samples. On the other hand, as discussed above, $\epsilon^{145}\text{Nd}$ may act as an excellent tracer for the epithermal neutron flux because $\epsilon^{145}\text{Nd}$ was measured to high accuracy (~ 5 ppm) along with the other Nd isotopes. Deviations of $\epsilon^{145}\text{Nd}$ from zero beyond the external precision of ± 5 ppm were measured only for the two most heavily irradiated KREEP samples 15386 and SaU 169. From these measurements, an estimate for Φ/Ξ of samples 15386 and SaU 169 was calculated by adjusting Φ/Ξ to yield $\epsilon^{145}\text{Nd} = 0$ in the 146/144 correction scheme. The resultant Φ/Ξ values are 1.1 for 15386 and 0.5 for SaU 169, respectively. The fractional effects $\Delta N_i/N_i$ on all neodymium isotopes were then calculated according to equation A2 given in Nyquist et al. (16) with Φ/Ξ set to 1.1 (except SaU 169 = 0.5) and published Pr, Nd, Sm and Eu concentrations for each sample. The $\Delta N_i/N_i$ values were then propagated through an exponential fractionation to yield final correction terms on $\epsilon^i\text{Nd}$.

The calculated Φ/Ξ values are within the range previously obtained (16), but more importantly, they are similar to 1.1 ± 0.2 at $180\text{g}/\text{cm}^2$ determined by direct measurements from the Apollo 17 Lunar Neutron Probe Experiment (LNPE) (23). It must be noted, however, that the LNPE measurements and theoretical considerations (17, 24) were performed in or for lunar soil. In soils, transport properties for neutrons are primarily determined by the major elements iron

and titanium. In a REE-rich KREEP basalt such as SaU 169 (sum REE = 1332 ppm), this approximation may break down because the macroscopic neutron cross section of the whole rock is dominated by Gd and Sm (Figure S8). The precise shape of the neutron energy spectrum in such REE-rich materials has not yet been measured directly.

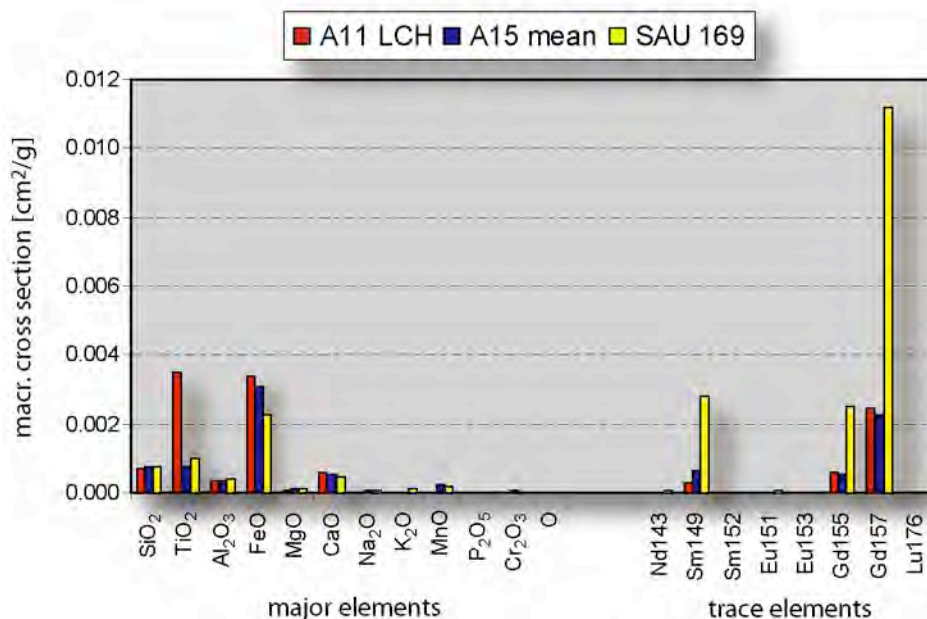


Figure S8: Comparison of the elemental contributions to the total macroscopic neutron capture cross section in samples SaU 169 and average Apollo 11 and 15 soils. In lunar soils, the shape of the neutron energy spectrum is mainly determined by neutron scattering and absorption of the major elements Fe and Ti. The soils have been used in various considerations of the lunar neutron spectrum (17, 21, 23, 24). KREEP, however, is markedly different and general approximations derived from the soils (like e.g. Lingenfelter’s work) might not be applicable.

The preferred fractionation and neutron fluence corrections for heavily irradiated samples

Neodymium has seven isotopes, of which ¹⁴²Nd and ¹⁴³Nd are radiogenic. In principle, this leaves 10 possible pairs of Nd isotopes to correct for instrumental mass fractionation.

Desirable for a ‘good’ pair are high isotopic abundance, a large spread in mass and absence of interferences. As pointed out above for the Sm isotopes, it is also important for irradiated samples to choose nuclides that are not significantly destroyed or produced by neutron irradiation processes. Table S5 presents a compilation of four different schemes for fractionation correction and corresponding neutron correction.

Sample	Correct. scheme	$\epsilon^{142}\text{Nd}$ measured	Corr. on $\epsilon^{142}\text{Nd}$	$\epsilon^{142}\text{Nd}$ final	$\epsilon^{144}\text{Nd}$ final	$\epsilon^{145}\text{Nd}$ final	$\epsilon^{146}\text{Nd}$ final	$\epsilon^{148}\text{Nd}$ final	$\epsilon^{150}\text{Nd}$ final
15386	146/144	-0.34 ± 0.05	0.145	-0.19 ± 0.05	$\equiv 0$	0.01 ± 0.02	$\equiv 0$	-0.07 ± 0.08	-0.09 ± 0.13
	146/145	0.32 ± 0.03	-0.565	-0.25 ± 0.03	-0.02 ± 0.04	$\equiv 0$	$\equiv 0$	-0.05 ± 0.05	-0.08 ± 0.11
	145/148	-0.08 ± 0.06	-0.195	-0.28 ± 0.06	-0.03 ± 0.03	$\equiv 0$	0.02 ± 0.02	$\equiv 0$	0.02 ± 0.14
	148/150	-0.27 ± 0.33	-0.016	-0.29 ± 0.33	-0.04 ± 0.24	-0.02 ± 0.15	0.01 ± 0.09	$\equiv 0$	$\equiv 0$
SaU 169	146/144	-0.32 ± 0.05	0.056	-0.26 ± 0.05	$\equiv 0$	0.02 ± 0.02	$\equiv 0$	-0.07 ± 0.02	-0.15 ± 0.08
	146/145	0.11 ± 0.07	-0.424	-0.32 ± 0.07	-0.04 ± 0.04	$\equiv 0$	$\equiv 0$	-0.05 ± 0.04	-0.07 ± 0.08
	145/148	-0.20 ± 0.06	-0.148	-0.34 ± 0.06	-0.05 ± 0.02	$\equiv 0$	0.02 ± 0.02	$\equiv 0$	-0.02 ± 0.03
	148/150	-0.39 ± 0.03	-0.013	-0.40 ± 0.03	-0.10 ± 0.05	-0.03 ± 0.06	-0.01 ± 0.03	$\equiv 0$	$\equiv 0$
LAP 02205	146/144				$\equiv 0$	0.00 ± 0.04	$\equiv 0$	-0.09 ± 0.07	0.00 ± 0.48
	146/145	-0.17 ± 0.04	0.016	-0.16 ± 0.04	0.01 ± 0.07	$\equiv 0$	$\equiv 0$	-0.10 ± 0.13	0.00 ± 0.60
	145/148	-0.05 ± 0.15	-0.119	-0.16 ± 0.15	-0.03 ± 0.04	$\equiv 0$	0.03 ± 0.04	$\equiv 0$	0.16 ± 0.43
	148/150	-0.19 ± 0.11	-0.041	-0.24 ± 0.11	0.29 ± 0.86	0.25 ± 0.66	0.20 ± 0.41	$\equiv 0$	$\equiv 0$
74275	146/144	0.06 ± 0.05	0.009	0.07 ± 0.05	$\equiv 0$	0.01 ± 0.05	$\equiv 0$	-0.05 ± 0.15	-0.15 ± 0.29
	146/145	0.11 ± 0.17	-0.064	0.05 ± 0.17	-0.01 ± 0.08	$\equiv 0$	$\equiv 0$	-0.05 ± 0.16	-0.15 ± 0.34
	145/148	0.04 ± 0.22	-0.022	0.02 ± 0.22	-0.02 ± 0.08	$\equiv 0$	0.02 ± 0.05	$\equiv 0$	-0.08 ± 0.13
	148/150	-0.17 ± 0.36	-0.002	-0.17 ± 0.36	-0.15 ± 0.21	-0.13 ± 0.15	-0.05 ± 0.11	$\equiv 0$	$\equiv 0$
70017	146/144	0.01 ± 0.05	0.006	0.02 ± 0.05	$\equiv 0$	0.00 ± 0.05	$\equiv 0$	-0.15 ± 0.15	-0.33 ± 0.29
	146/145	0.06 ± 0.17	-0.046	0.01 ± 0.17	0.01 ± 0.08	$\equiv 0$	$\equiv 0$	-0.16 ± 0.16	-0.31 ± 0.34
	145/148	-0.14 ± 0.22	-0.016	-0.16 ± 0.22	-0.06 ± 0.08	$\equiv 0$	0.05 ± 0.05	$\equiv 0$	-0.02 ± 0.13
	148/150	-0.26 ± 0.36	-0.001	-0.27 ± 0.36	-0.13 ± 0.21	-0.02 ± 0.15	0.02 ± 0.11	$\equiv 0$	$\equiv 0$
15555	146/144	-0.16 ± 0.05	0.024	-0.13 ± 0.05	$\equiv 0$	0.01 ± 0.05	$\equiv 0$	0.08 ± 0.15	0.95 ± 0.29
	146/145	0.01 ± 0.17	-0.179	-0.17 ± 0.17	0.00 ± 0.08	$\equiv 0$	$\equiv 0$	0.10 ± 0.16	0.87 ± 0.34
	145/148	0.03 ± 0.22	-0.062	-0.04 ± 0.22	0.06 ± 0.08	$\equiv 0$	-0.04 ± 0.05	$\equiv 0$	0.71 ± 0.13
	148/150	2.08 ± 0.36	-0.005	2.07 ± 0.36	1.43 ± 0.21	1.07 ± 0.15	0.67 ± 0.11	$\equiv 0$	$\equiv 0$

Table S5: Final $\epsilon^i\text{Nd}$ of all samples using four different correction schemes for mass fractionation during TIMS measurements and subsequent correction for neutron irradiation effects. The correction terms for $\epsilon^{142}\text{Nd}$ (column 4 in red) are dependent on the fractionation correction scheme used. Note the large correction on 146/145-normalized data.

A $^{146}\text{Nd}/^{145}\text{Nd}$ correction scheme for the fractionation correction of Nd-isotopes could be potentially favorable, because it should be relatively free of the effects of thermal neutron irradiation (Table S4). However, the $^{146}\text{Nd}/^{145}\text{Nd}$ correction scheme does not avoid irradiation effects because of the $^{145}\text{Nd}(n,\gamma)^{146}\text{Nd}$ reaction with an epithermal capture cross section of 231 barns (Table S4). As outlined above, the ratio of the thermal to epithermal neutron fluences Φ/Ξ is about unity. Because ^{145}Nd is destroyed and ^{146}Nd is generated in this reaction with the same (high) cross section, the combined effect on the $^{146}\text{Nd}/^{145}\text{Nd}$ ratio is larger than ratios including ^{144}Nd , ^{148}Nd , or ^{150}Nd , and thus results in the largest correction terms on $\epsilon^{142}\text{Nd}$ (cf. Table S5).

Despite this potential complication, the corrections for neutron irradiation result in identical $\epsilon^{142}\text{Nd}$ values for both the $^{146}\text{Nd}/^{144}\text{Nd}$ and the $^{146}\text{Nd}/^{145}\text{Nd}$ correction schemes within error (Figure S9). Moreover, the $\epsilon^{144}\text{Nd}$, $\epsilon^{145}\text{Nd}$, $\epsilon^{146}\text{Nd}$, $\epsilon^{148}\text{Nd}$, and $\epsilon^{150}\text{Nd}$ values in Table S5 are within error or very close to zero and show no residual correlation with $\epsilon^{149}\text{Sm}$, and thus confirm a successful neutron correction scheme (Figure S10).

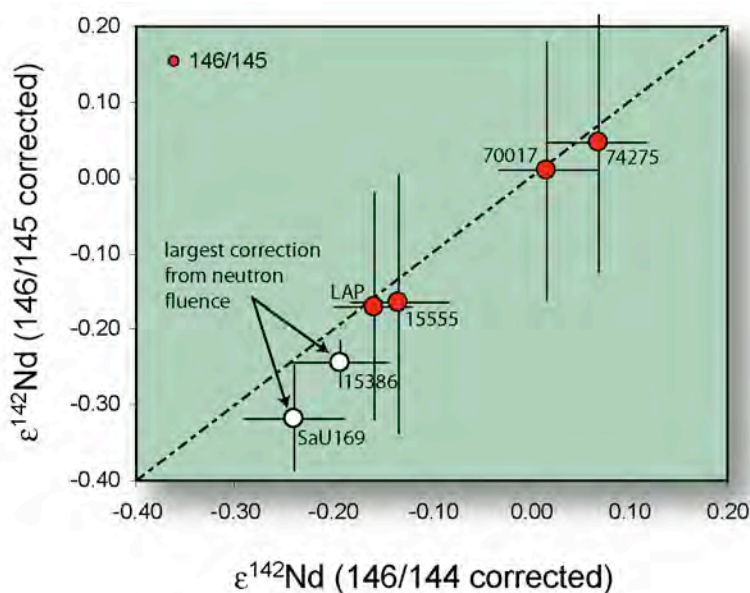


Figure S9: Comparison of final $\epsilon^{142}\text{Nd}$ values after correction for mass fractionation and neutron irradiation using a 146/144 correction (x-axis) and a 146/145 correction scheme (y-axis). The broken line represents a 1:1 correlation.

For the less irradiated samples (red dots) the results are within error identical. The two more irradiated KREEP samples have slightly lower $\epsilon^{142}\text{Nd}$ in the 146/145 scheme, and we therefore used an average of the two KREEP samples for the discussion in the manuscript.

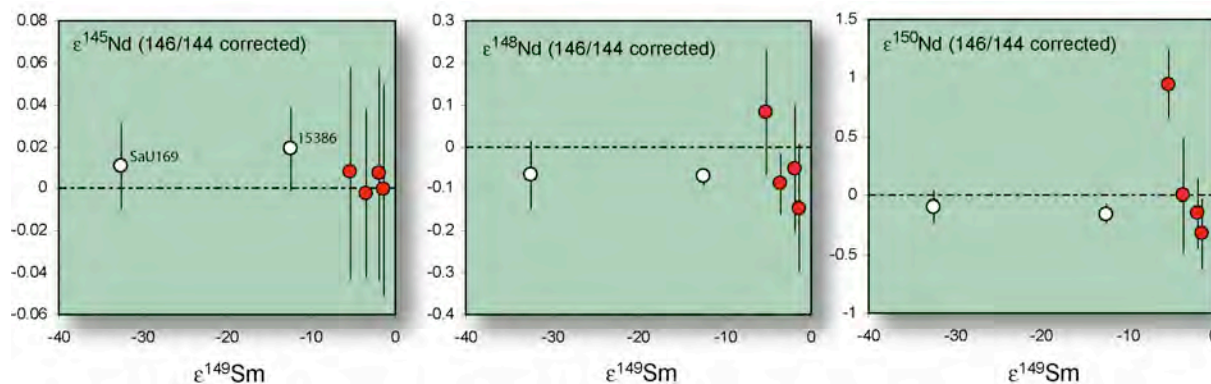


Figure S10: $\epsilon^{145, 148, 150}\text{Nd}$ versus $\epsilon^{149}\text{Sm}$ for all samples after correction for neutron irradiation. No residual correlation with $\epsilon^{149}\text{Sm}$ is observed, confirming a successful correction scheme.

One way to unambiguously quantify the effects of neutron irradiation is normalization of the raw data to $^{148}\text{Nd}/^{150}\text{Nd}$ (Table S5). Because of the small thermal and epithermal cross sections of ^{148}Nd and ^{150}Nd (Table S4), the normalized data should directly reflect the isotope anomalies in proportion to their respective neutron cross sections. However, because of the lower isotopic abundance of ^{148}Nd and ^{150}Nd compared to ^{144}Nd and ^{146}Nd , and a much larger spread in mass between normalizing and measured isotopes, the error on the analytical reproducibility increases significantly and makes this scheme unsuitable for the detection of small anomalies in $\epsilon^{142}\text{Nd}$ (Table S5).

Because the correction schemes using $^{146}\text{Nd}/^{144}\text{Nd}$, $^{146}\text{Nd}/^{145}\text{Nd}$, $^{145}\text{Nd}/^{148}\text{Nd}$ in Table S5 give similar results for $\epsilon^{142}\text{Nd}$ after neutron correction, we report a mean of these three for the final corrected $\epsilon^{142}\text{Nd}$ values for the KREEP samples 15386 (-0.24 ± 0.07 , 2σ) and SaU 169 (-0.30 ± 0.07 , 2σ) in the paper. Considering the potential complications in the corrections for

these two samples, it is our opinion that this is the most conservative approach for obtaining the true $\epsilon^{142}\text{Nd}$. For the other four lunar samples, where the differences in the correction schemes are smaller than the analytical uncertainty of ~ 5 ppm (Table S3), the more precise value using the $^{146}\text{Nd}/^{144}\text{Nd}$ scheme is reported.

Alternative models for the generation of negative $\epsilon^{142}\text{Nd}$ of chondrites

It has been suggested that some or all of the differences in $\epsilon^{142}\text{Nd}$ between chondrites and the terrestrial standard reported in Boyet and Carlson (12) might be generated by processes other than radiogenic ingrowth of now extinct ^{146}Sm from parent sources having different bulk Sm/Nd ratios. Instead, these differences may result from inhomogeneous distribution of r- and s-process nuclides in the fractions of primitive chondrites measured, or from small fractions having a different Sm/Nd ratio, and therefore do not represent the true bulk parent Nd isotope composition (13, 25). If chondrites actually have a bulk average of $\epsilon^{142}\text{Nd} = 0$ rather than -0.2 (12), then the premise of a chondritic Moon that is distinct from the terrestrial Nd isotope standard is based upon false conclusions.

In general, nucleosynthetic anomalies are almost invariably restricted to refractory inclusions in chondrites (26). How a nucleosynthetic ^{142}Nd excess could be correlated with ^{146}Sm is unclear (27). The isotopic composition of s-process Nd is different from that of the terrestrial standard (28, 29). If the s-process Nd is hosted in a separate phase in chondrites such as SiC, which may be chemically resistant during sample decomposition or inhomogeneously distributed on the scale of the fraction analyzed, then there is a possibility that a measured Nd isotope composition is not representative for that of the bulk chondrite. This is illustrated in a model calculation (Fig. S11). The fact that chondrites show *both* negative $\epsilon^{142}\text{Nd}$ and $\epsilon^{150}\text{Nd}$ is inconsistent with the assumption that these anomalies reflect incomplete dissolution or unrepresentative sam-

pling. Further support comes from recent Os isotope data of bulk chondrites (30). This study found that bulk H Group ordinary chondrites did not have any evidence for non-representative Os isotopic compositions as a result of presolar components that were not accessed during digestion or from inhomogeneous distribution for the fractions measured. The implications of these data are that bulk compositions of these meteorites represent the composition of the averaged solar nebula from which they were derived. Boyet and Carlson measured Nd in three ordinary chondrites including replicates of two (12). The average for these three is -0.20 ± 0.12 (2σ), identical to the average for all chondrite data reported, including primitive carbonaceous chondrites. Further, the eucrite data reported in Boyet and Carlson are consistent with a bulk source of the eucrite parent body being at $\epsilon^{142}\text{Nd} \sim -0.2$, and is strong evidence that supports a bulk chondritic value at -0.2 , consistent with the ordinary chondrite data.

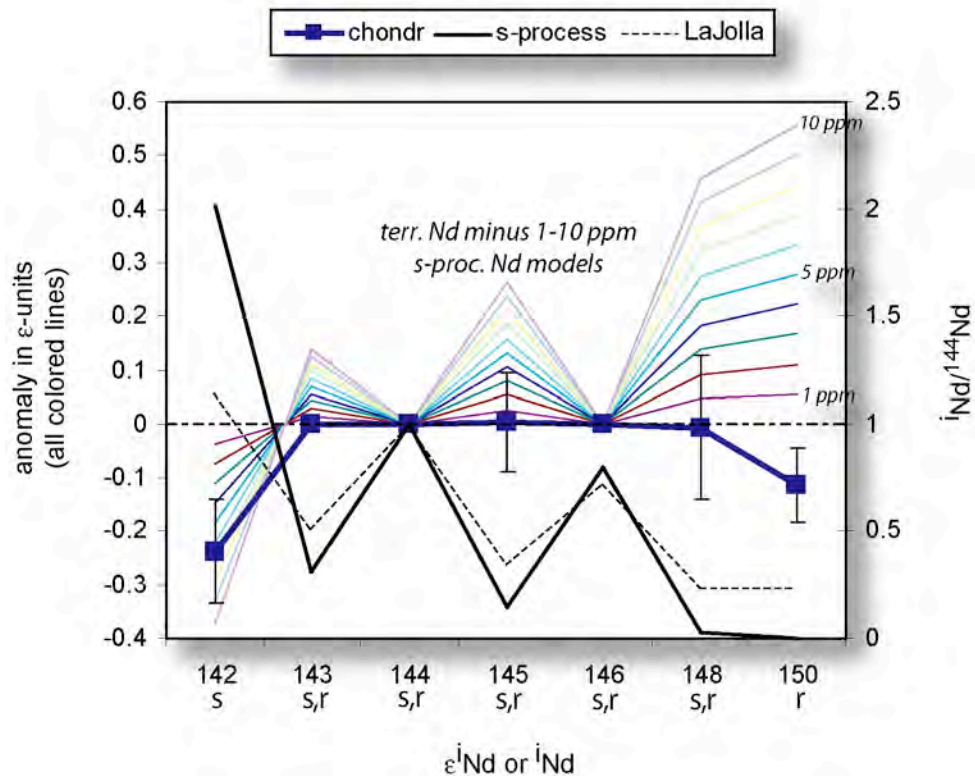


Figure S11: The average chondrite composition of Boyet and Carlson (blue squares) is plotted as $\epsilon^{144}\text{Nd}$ -deviations from the terrestrial La Jolla Nd isotope standard with $\epsilon^{144}\text{Nd} = 0$ (primary, i.e. left y-axis). Error bars for average chondrite are $\pm 2\sigma$. Also plotted are the calculated compositions of La Jolla minus 1 to 10 ppm of s-process Nd (col-

ored thin lines). The isotopic abundances of La Jolla (black broken line) and s-process Nd (black bold line) normalized to ^{144}Nd are plotted for comparison (secondary, i.e. right y-axis). If the negative $\epsilon^{142}\text{Nd}$ in chondrites is the result of missing s-process isotopes, then coupled positive anomalies at 145, 148, and 150 are expected. The chondrite data shows that this is not observed and thus the negative $\epsilon^{142}\text{Nd}$ of ~ -0.2 in chondrites is likely a representation of the bulk source materials.

Choosing an initial $^{146}\text{Sm}/^{144}\text{Sm}$

The equations used for modeling the neodymium isotope evolution of the Moon require a well-constrained $^{146}\text{Sm}/^{144}\text{Sm}$ at t_0 - the onset of nebular condensation [~ 4567 m.y. (31)]. The initial $^{146}\text{Sm}/^{144}\text{Sm}$ ratios derived from internal isochrons of differentiated meteorites likely do not represent the value at t_0 , but instead at some later time [for a summary of available data see Table 2 of (32)]. A $^{146}\text{Sm}/^{144}\text{Sm} = 0.0075 \pm 0.0027$ that is derived from chondrules and chondritic phosphate fractions (10) was chosen in this study, because the data from chondrites should more closely pinpoint the value of $^{146}\text{Sm}/^{144}\text{Sm}$ at the time of solar system formation. The initial $^{146}\text{Sm}/^{144}\text{Sm}$ at the time of Moon formation can then be calculated as $^{146}\text{Sm}/^{144}\text{Sm}(\Delta t) = 0.0075 * \exp(-\lambda_{146} * \Delta t)$ and equals 0.0061 to 0.0054 for formation ages Δt of the Moon ranging from 30 to 50 m.y. after t_0 .

Because ^{146}Sm is decaying with time, later Sm/Nd-fractionations will give shallower slopes in a $\epsilon^{142}\text{Nd}-\epsilon^{143}\text{Nd}$ isotope diagram (this relationship is illustrated by the slope of the lines in our Figure 3 in the manuscript). A lower initial $^{146}\text{Sm}/^{144}\text{Sm}$ ratio at solar system formation has the same consequence as a later fractionation event. The uncertainty in the initial solar system $^{146}\text{Sm}/^{144}\text{Sm}$ ratio (± 0.0027) thus propagates directly to the estimation of the lunar formation interval and translates to formation intervals ranging from 148 to 260 m.y. after t_0 . However, this may be a large overestimation of the true uncertainty. The most precise determination of the initial $^{146}\text{Sm}/^{144}\text{Sm}$ ratio in early solar system material comes from angrite LEW 86010 with 0.0076

± 0.0009 at 4558 m.y. (33). This datum extrapolates to 0.0081 ± 0.0009 at $t_0 = 4567$ m.y. and overlaps with the result derived from chondrites, and is likely a better estimate of the error interval associated with the solar system initial $^{146}\text{Sm}/^{144}\text{Sm}$. Using $^{146}\text{Sm}/^{144}\text{Sm} = 0.0081 \pm 0.0009$ raises the formation interval slightly to 226 m.y. with an error interval of $^{+15}_{-17}$ m.y. This result is very similar to the 215^{+23}_{-21} m.y. derived from the regression analysis favored here, and shows that the error on the initial $^{146}\text{Sm}/^{144}\text{Sm}$ ratio does not introduce a significant additional uncertainty. It is important to emphasize that the error associated with the initial $^{146}\text{Sm}/^{144}\text{Sm}$ ratio does not affect the estimate of the initial lunar $\epsilon^{142}\text{Nd}$ (which forms the core argument for a chondritic Moon), because the isochrons will only rotate around the chondritic intersection point in Figure 2A, but not shift vertically. The primary conclusion drawn from these data, that the Moon has $\epsilon^{142}\text{Nd}$ composition close to that of chondrites and different to that of the terrestrial standard is therefore unaffected by the choice of $^{146}\text{Sm}/^{144}\text{Sm}$.

Equations and additional data used for calculations

$$\left(\frac{^{143}\text{Nd}}{^{144}\text{Nd}}\right)_{t_1} = \left(\frac{^{143}\text{Nd}}{^{144}\text{Nd}}\right)_{\text{CHUR, today}} + \left(\frac{^{147}\text{Sm}}{^{144}\text{Nd}}\right)_{\text{CHUR, today}} \times (1 - e^{-\lambda_{147}t_1})$$

$$+ \left(\frac{^{147}\text{Sm}}{^{144}\text{Nd}}\right)_{t_1} \times (e^{\lambda_{147}t_1} - e^{\lambda_{147}t_2})$$

$$\left(\frac{^{142}\text{Nd}}{^{144}\text{Nd}}\right)_{t_1} = \left(\frac{^{142}\text{Nd}}{^{144}\text{Nd}}\right)_{\text{CHUR, today}} - \left(\frac{^{146}\text{Sm}}{^{144}\text{Sm}}\right)_{\text{CHUR, } t_0} \times \left(\frac{^{144}\text{Sm}}{^{147}\text{Sm}}\right)_{\text{today}}$$

$$\times \left[\left(\frac{^{147}\text{Sm}}{^{144}\text{Nd}}\right)_{\text{CHUR, today}} \times e^{-\lambda_{146}(t_0-t_1)} + \left(\frac{^{147}\text{Sm}}{^{144}\text{Nd}}\right)_{t_1} \times (e^{-\lambda_{146}(t_0-t_2)} - e^{-\lambda_{146}(t_0-t_1)}) \right]$$

Equations S1, S2: 2-stage model for the isotopic evolution of neodymium. $(^{143}\text{Nd}/^{144}\text{Nd})_{\text{CHUR, today}} = 0.512637$, $(^{147}\text{Sm}/^{144}\text{Nd})_{\text{CHUR, today}} = 0.1964$ and $(^{146}\text{Sm}/^{144}\text{Sm})_{\text{CHUR, } t_0} = 0.0075$ were taken from (10), $(^{144}\text{Sm}/^{147}\text{Sm})_{\text{today}} = 0.205022$ (our Sm standard measurements), $\lambda_{147} = 6.54 \times 10^{-12} \text{ yr}^{-1}$, $\lambda_{146} = 6.74 \times 10^{-9} \text{ yr}^{-1}$ and $t_0 = 4567 \text{ m.y.}$, $t_1 = \text{time of LMO crystallization}$, $t_2 = \text{time of basalt crystallization}$.

$$\left(\frac{^{143}\text{Nd}}{^{144}\text{Nd}}\right)_{t_1} = \left(\frac{^{143}\text{Nd}}{^{144}\text{Nd}}\right)_{\text{CHUR, today}} + \left(\frac{^{147}\text{Sm}}{^{144}\text{Nd}}\right)_{\text{CHUR, today}} \times (1 - e^{-\lambda_{147}t_1})$$

$$+ \left(\frac{^{147}\text{Sm}}{^{144}\text{Nd}}\right)_{t_1} \times (e^{\lambda_{147}t_1} - e^{\lambda_{147}t_2}) + \left(\frac{^{147}\text{Sm}}{^{144}\text{Nd}}\right)_{t_2} \times (e^{\lambda_{147}t_2} - e^{\lambda_{147}t_3})$$

$$\left(\frac{^{142}\text{Nd}}{^{144}\text{Nd}}\right)_{t_1} = \left(\frac{^{142}\text{Nd}}{^{144}\text{Nd}}\right)_{\text{CHUR, today}} - \left(\frac{^{146}\text{Sm}}{^{144}\text{Sm}}\right)_{\text{CHUR, } t_0} \times \left(\frac{^{144}\text{Sm}}{^{147}\text{Sm}}\right)_{\text{today}}$$

$$\times \left[\left(\frac{^{147}\text{Sm}}{^{144}\text{Nd}}\right)_{\text{CHUR, today}} \times e^{-\lambda_{146}(t_0-t_1)} + \left(\frac{^{147}\text{Sm}}{^{144}\text{Nd}}\right)_{t_1} \times (e^{-\lambda_{146}(t_0-t_2)} - e^{-\lambda_{146}(t_0-t_1)}) \right]$$

$$+ \left(\frac{^{147}\text{Sm}}{^{144}\text{Nd}}\right)_{t_2} \times (e^{-\lambda_{146}(t_0-t_3)} - e^{-\lambda_{146}(t_0-t_2)})$$

Equations S3, S4: 3-stage model for a depleted Moon. CHUR parameters, $(^{144}\text{Sm}/^{147}\text{Sm})_{\text{today}}$ and decay constants as before, $(^{147}\text{Sm}/^{144}\text{Nd})_{t_1} = 0.2146$ and $t_1 = 4537 \text{ m.y.}$ (12). $t_2 = \text{time of LMO crystallization}$, $t_3 = \text{time of basalt crystallization}$.

	LAP 02205	SAU 169	15386	74275	70017	15555
CHUR source						
$t_{\text{form}}=50$ m.y.	0.2025	0.1658	0.1826	0.2514	0.2558	0.2146
$t_{\text{form}}=200$ m.y.	0.2032	0.1560	0.1786	0.2642	0.2690	0.2173
Depleted source						
$t_{\text{form}}=50$ m.y.	0.2022	0.1652	0.1820	0.2509	0.2554	0.2143
$t_{\text{form}}=200$ m.y.	0.2007	0.1493	0.1726	0.2594	0.2644	0.2143

Table S6: $^{147}\text{Sm}/^{144}\text{Nd}$ ratios for sources formed at 50 and 200 m.y. after solar system formation, calculated based on age and initial $\epsilon^{143}\text{Nd}$ of the samples.

References

1. E. Gnos *et al.*, *Science* **305**, 657 (2004).
2. K. Rankenburg, A. D. Brandon, M. D. Norman, K. Righter, *METSOC* **68th**, #5294 (2005).
3. M. Anand *et al.*, *GCA* **70**, 246 (2005).
4. W. M. White, J. Patchett, *EPSL* **67**, 167 (1984).
5. M. Rehkaemper, M. Gaertner, S. J. G. Galer, S. L. Goldstein, *Chemical Geology* **129**, 201 (1996).
6. G. Caro, B. Bourdon, J.-L. Birck, S. Moorbath, *GCA* **70**, 164 (2006).
7. G. Caro, B. Bourdon, J.-L. Birck, S. Moorbath, *Nature* **423**, 428 (2003).
8. G. J. Wasserburg, S. B. Jacobsen, D. J. Depaolo, M. T. McCulloch, T. Wen, *GCA* **45**, 2311 (1981).
9. S. R. Hart, *Nature* **309**, 753 (1984).
10. Y. Amelin, E. Rotenberg, *EPSL* **223**, 267 (2004).
11. P. J. Patchett, J. D. Vervoort, U. Soederlund, V. J. M. Salters, *EPSLs* **222**, 29 (2004).
12. M. Boyet, R. W. Carlson, *Science* **309**, 576 (2005).
13. R. Andreasen, M. Sharma, *EOS Transactions, American Geophysical Union* **86**, Fall Meet. Suppl. (2005).
14. W. C. Feldman, W. V. Boynton, D. M. Drake, in *Remote Geochemical Analysis: Elemental and Mineralogical Composition* C. M. Pieters, P. J. Englert, Eds. (Cambridge University Press, New York, 1993) pp. 213-234.
15. O. Eugster, F. Tera, D. S. Burnett, G. J. Wasserburg, *EPSL* **8**, 20 (1970).
16. L. E. Nyquist *et al.*, *GCA* **59**, 2817 (1995).
17. R. E. Lingenfelter, E. H. Canfield, V. E. Hampel, *EPSL* **16**, 355 (1972).
18. (OECD Nuclear Energy Agency, France, <http://www.nea.fr/html/dbdata/JEFF/>).
19. D. E. Cullen. (report IAEA-NDS-39, Rev. 12, 2004).
20. G. P. Russ, *EPSL* **13**, 384 (1972).
21. H. Hidaka, M. Ebihara, S. Yoneda, *MAPS* **35**, 581 (2000).
22. D. G. Sands, J. R. de Laeter, K. J. R. Rosman, *EPSL* **186**, 335 (2001).
23. D. S. Woolum, D. S. Burnett, M. Furst, J. R. Weiss, *The Moon* **12**, 231 (1975).
24. I. Leya, R. Wieler, A. N. Halliday, *GCA* **67**, 529 (2003).
25. M. C. Ranen, S. B. Jacobsen, *EOS Transactions, American Geophysical Union* **86**, Fall Meet. Suppl. (2005).
26. J. L. Birck, in *Geochemistry of Non-Traditional Stable Isotopes* C. M. Johnson, B. L. Beard, F. Albarède, Eds. (The Mineralogical Society of America, Washington, DC, 2004), vol. 55, pp. 25-64.
27. A. Prinzhofer, D. A. Papanastassiou, G. J. Wasserburg, *GCA* **56**, 797 (1992).
28. S. Richter, U. Ott, F. Begemann, *LPSC* **23th**, 1147 (1992).
29. K. H. Guber, R. R. Spencer, P. E. Koehler, R. R. Winters, *Phys. Rev. Lett.* **78**, 2704 (1997).
30. A. D. Brandon, M. Humayun, I. S. Puchtel, I. Leya, M. Zolensky, *Science* **309**, 1233 (2005).
31. Y. Amelin, A. N. Krot, I. D. Hutcheon, A. A. Ulyanov, *Science* **297**, 1678 (2002).
32. R. W. Carlson, G. W. Lugmair, in *Origin of the Earth and Moon* R. M. Canup, K. Righter, Eds. (The University of Arizona Press, Tucson, 2000) pp. 25-44.
33. L. E. Nyquist, B. Bansal, H. Wiesmann, C. Y. Shih, *Meteoritics* **29**, 872 (1994).